

Gigayear stability of cratonic edges controls global distribution of sediment-hosted metals

Karol Czarnota^{*,1,2}, Mark J. Hoggard^{*,3,4}, Fred D. Richards³, David L. Huston¹ & A. Lynton Jaques²

1. Geoscience Australia, GPO Box 378, Canberra ACT 2601, Australia.
2. Research School of Earth Sciences, Australian National University, Canberra, ACT 0200, Australia
3. Department of Earth and Planetary Sciences, Harvard University, 20 Oxford Street, Cambridge, MA 02138, USA.
4. Lamont-Doherty Earth Observatory, Columbia University, 61 Rte 9W, Palisades, NY 10964, USA.

*karol.czarnota@ga.gov.au; mark_hoggard@fas.harvard.edu

1 **Sustainable development and transition to a clean-energy economy is placing ever-increasing de-**
2 **mand on global supplies of base metals (copper, lead, zinc and nickel). Alarminglly, this demand**
3 **is outstripping the present rate of discovery of new deposits, with significant shortfalls forecast in**
4 **the coming decades. Thus, to maintain growth in global living standards, dramatic improvements**
5 **in exploration success rate are an essential goal of the geoscience community. Significant quantities**
6 **of base metals have been deposited by low-temperature hydrothermal circulation within sedimen-**
7 **tary basins over the last 2 billion years. Despite over a century of research, relationships between**
8 **these deposits and geological structures remain enigmatic. Here, for the first time, we show that**
9 **85% of sediment-hosted base metals, including all giant deposits (> 10 megatonnes of metal), occur**
10 **within 200 km of the edges of thick lithosphere, mapped using surface wave tomography and a**
11 **parameterisation for anelasticity at seismic frequencies. This remarkable observation implies long-**
12 **term lithospheric edge stability and a genetic link between deep Earth processes and near-surface**
13 **hydrothermal mineral systems. This result provides an unprecedented global framework for iden-**
14 **tifying fertile regions for targeted mineral exploration, reducing the search-space for new deposits**
15 **by two-thirds on this lithospheric thickness criterion alone.**

16 Consumption of base metals over the next ~25 years is set to exceed the total produced in human history to
17 date.^{1,2} Moreover, trace metals (e.g. cobalt, indium and germanium) are often produced as by-products of base
18 metal mining and are essential in many high-tech applications.³ A growing concern is that the rate of exploitation
19 of existing reserves is outstripping discovery of new deposits, despite exploration expenditure tripling during the
20 2005–2012 minerals boom.^{1,2} To reverse this worrying trend, improved techniques for locating new deposits are
21 required, particularly those buried under shallow sedimentary cover or ice. Initial area selection at continental
22 scales is arguably the most important stage of mineral exploration, as successful identification of fertile regions can
23 compensate for many subsequent exploration errors.⁴

24 **Global Deposit Classification**

25 Over the last two decades, ore deposit research has progressed from documentation and classification towards
26 a more holistic understanding of factors controlling generation and preservation of mineral deposits.^{5,6} Classifi-
27 cation schemes have identified six major base metal deposit types, based on variations in mineral assemblages,
28 host lithology, structural architecture and geological setting. Three of these are associated with magmatic pro-
29 cesses: porphyry copper (contains ~65% of all known copper); magmatic nickel-copper-platinum group elements
30 (~45% nickel, ~3% copper); and volcanic-hosted massive sulphide copper-lead-zinc (~6% copper, ~23% lead,
31 ~39% zinc). Mineral systems analysis has resulted in a growing acceptance that the spatial distribution of such
32 deposits associated with magmatic processes is controlled by lithospheric-scale structure.^{4,7,8}

33 The other three deposit types are associated with low-temperature hydrothermal circulation in sedimentary
34 basins: sedimentary copper (Cu-sed; contains ~20% of all known copper); clastic-dominated lead-zinc (PbZn-CD),
35 commonly also referred to as sedimentary exhalative (~43% of all lead and ~33% of zinc); and Mississippi Valley-
36 type lead-zinc (PbZn-MVT; ~25% lead, ~22% zinc). Most assessments to date have focused on the genesis of these
37 sediment-hosted deposits within the context of Earth's secular evolution as well as past tectonic and geographic
38 settings.^{9,10,11,12} However, the first-order geological control on their spatial distribution throughout the continents
39 is unknown, severely limiting predictive power for identifying new targets. A classic example comes from the
40 Carpentaria Zinc Belt in northern Australia, which contains several world class PbZn-CD deposits formed between
41 1.8–1.4 Ga (Figure 1a). These deposits lie along an arcuate trend that runs oblique to mapped geology and crustal
42 geological boundaries, as demonstrated by gravity and magnetic datasets.¹³ This linear distribution hints at an
43 underlying regional-scale control. Given the absence of a clear crustal relationship, we therefore investigate both
44 regional and global-scale links between base-metal deposits and the most fundamental shallow mantle structure –
45 the lithosphere-asthenosphere boundary (LAB).

46 **Relationship with Lithospheric Structure**

47 We begin by collating global inventories of the six aforementioned major base-metal systems from published sources
48 (Supplementary Information). We next refine a method¹⁴ for mapping the thermal LAB from seismic tomogra-
49 phy, taking into consideration recent laboratory experiments¹⁵ concerning the effect of anelasticity on shear-wave
50 velocities (Methods). This benchmarking procedure is necessary due to substantial variability in the results of
51 different tomography models. A high resolution regional map over Australia is obtained from the FR12 model¹⁶
52 and is calibrated using nine local paleogeotherms derived from thermobarometry of mantle peridotite xenoliths
53 and xenocrysts. To expand our analysis to other continents, a global LAB is also produced using SL2013sv to-
54 mography¹⁷ and calibrated using multiple constraints, including the latest thermal structure of cooling oceanic
55 lithosphere.¹⁸ This global LAB exhibits a bi-modal thickness distribution, with peaks at 80 km and 180 km,
56 separated by a minimum at 150 km (Supplementary Information).

57 Inspection of the Australian model reveals a striking correlation between major sediment-hosted mineral deposits
58 and the edge of thick lithosphere, defined here by the 170 km thickness contour (Figure 1b). Major PbZn-CD and

59 sedimentary copper deposits in the Carpentaria Zinc Belt overlie this contour, which runs obliquely to geological
60 boundaries, such that intersections between these two features consistently coincide with deposit locations. This
61 behaviour is particularly useful for highlighting new prospective regions for exploration. Other observables that
62 correlate with this lithospheric thickness change include variations in lead isotopes from Proterozoic galena and
63 pyrite minerals,¹⁹ a topographic ridge and the western extent of Cretaceous marine sediments (Figure 1a). These
64 latter two associations demonstrate the post-Proterozoic stability of this edge and its influence on local geology
65 and topography. There is also a strong relationship with iron-oxide-copper-gold deposits, including the Olympic
66 Dam mine in south Australia (84 Mt of copper, largest known uranium resource). However, lack of consensus over
67 global classification schemes means that we have limited analysis of this deposit type to Australia.

68 Extension to a global analysis confirms the strength of this relationship (Figure 2). There is a remarkable link
69 between the 170 km lithospheric thickness contour and location of large deposits that holds regardless of deposit
70 age, which spans at least the last 2 billion years. Surprisingly, given results of previous studies,⁸ deposits associated
71 with magmatic systems generally do not follow this simple pattern (Supplementary Information).

72 To quantify these visual relationships, the shortest distance is calculated between each deposit and the 170 km
73 LAB thickness contour and results are plotted in a cumulative distribution function (CDF). Weighting deposits
74 by the mass of contained metal and substituting the Australian LAB from the global model with our regionally
75 enhanced version substantially improves the correlation for PbZn-CD (Figure 3a). Globally, we observe that
76 ~ 90% of sedimentary copper, ~ 90% of clastic-dominated lead-zinc and ~ 70% of Mississippi Valley-type lead-
77 zinc resources are located within 200 km of the 170 km LAB thickness contour (Figure 3b). This region corresponds
78 to only ~ 36% of continental surface area. Given that this swath width is similar to the ~ 280 km node spacing in
79 SL2013sv, tighter constraints are only possible with higher resolution tomography models. The significance of this
80 result is examined using the *two-sample Kolmogorov-Smirnov test*²⁰ which estimates that the probability of these
81 sediment-hosted deposits representing random continental locations is less than 1 in 10¹² (Methods).

82 Despite this general association, there are some notable exceptions. Minor PbZn-CD outliers occur in Europe,
83 the Caribbean, Indonesia and east China. Anomalous PbZn-MVT deposits are found in Ireland, east China and
84 along the Tethys subduction zone across Europe, whilst minor sedimentary copper deposits occur in southwestern
85 North America and southern South America. Not all outliers were necessarily anomalies at the time of ore forma-
86 tion. The majority now occur in accretionary terranes, whereby plate tectonic processes may have rifted segments
87 off thick lithosphere and transported them into subduction zone settings. Other areas, such as east China, are
88 known to have undergone lithospheric thinning some time after deposit formation, based on thermobarometric
89 constraints.²¹

90 Regardless of age, sediment-hosted base-metal deposits predominantly cluster on the edges of present-day thick
91 lithosphere. Therefore, many of these lithospheric steps appear to be remarkably robust on billion-year timescales,
92 despite the assembly and disaggregation of several supercontinents, impacts of large igneous provinces and the
93 erosional effect of edge-driven convection. Deposits in northwestern North America span ages ~ 1.5–0.5 Ga,
94 pointing to the stability and importance of this boundary in localising multiple deformation and ore-forming
95 processes.

96 Mineral System Implications

97 The majority of sediment-hosted base metal deposits are found in failed rift and passive margin settings.^{9,10} Our
98 results indicate that the edges of thick lithosphere place first-order controls on the genesis of these extensional basins
99 and their associated mineral systems (Figure 4). It is generally agreed that basin-scale hydrothermal circulation is
100 required to scavenge sufficient metals to form giant deposits.²² Metals are mobilised and transported by oxidised
101 brines with moderate temperatures (80–250°C) and moderate-to-high salinity (10–30 wt.% NaCl), limiting their
102 maximum age to the Great Oxidation Event at 2.4 Ga.^{9,10} These fluids are sourced from evaporites at low latitudes
103 and remain buffered as they pass through voluminous oxidised terrestrial sediments, allowing them to scavenge
104 lead from arkosic sandstones and felsic volcanics, as well as copper and zinc from mafic rocks.^{9,10} The latter
105 are more prevalent in distal parts of the basin where extension and decompression melting rates are greatest.
106 Transport along faults focuses these fluids into oxidation-reduction interfaces, such as distal-facies black shales,
107 where metals precipitate.¹¹ The optimal juxtaposition of these elements for efficient mineralisation is fundamentally
108 controlled by the lithospheric thickness change imparted by rifting. This transition marks the confluence between
109 oxidising terrestrial environments on thick lithosphere and reducing marine settings above thinner lithosphere.
110 The adjacent cratons provide a bountiful source of oxidised sediments and extensive low-elevation platforms that
111 enhance evaporite formation. Proximal land masses also promote restricted marine settings that are favourable for
112 euxinic water conditions and deposition of reducing shales high in organic carbon. Metal precipitation at these sites
113 is ineffective when fluid temperatures exceed $\sim 250^\circ\text{C}$.¹¹ Reduced geothermal gradients associated with thicker
114 lithosphere extend the depth range for sourcing brines cooler than this threshold, thereby maximising the depth
115 extent of the metal scavenging window.

116 From a geodynamical perspective, these lithospheric edges represent rheological contrasts that focus strain
117 and localise repeated cycles of extensional deformation and basin contraction, thereby controlling both the spatial
118 distribution of required lithologies and the focusing of mineralising fluids.^{23,24} Intercalation of necessary proximal
119 and distal facies components is further modulated by transient vertical motions, generally thought to be associated
120 with edge driven convection across lithospheric steps.²⁵ Finally, a setting on the edge of thick lithosphere enhances
121 the preservation potential of deposits through subsequent orogenic events and supercontinent cycles. For example,
122 the 1.7 Ga Broken Hill deposit in Australia (world's largest lead deposit) has been metamorphosed to amphibolite–
123 granulite facies, yet survives on the edge of the Curnamona part of the South Australian Craton.

124 In contrast to sediment-hosted base-metals, magmatic deposits do not show such a strong association with
125 the edge of thick lithosphere (Supplementary Material). Porphyry copper deposits are predominantly Cenozoic in
126 age and generally on thin lithosphere (≤ 100 km). Their formation in subduction zone settings at shallow crustal
127 depths leads to poor preservation potential within the geological record, making this association unsurprising.
128 Volcanogenic massive sulphides have a relatively continuous, though pulsed, age distribution from 3.5 Ga to present.
129 Their generation is thought to require moderate-degree partial melting of hydrated mantle in back-arc settings.²⁶
130 We observe that they spatially occur randomly on thick and thin lithosphere, but exhibit systematic temporal
131 ordering, with the oldest positioned over thick lithosphere rimmed by progressively younger deposits, consistent

132 with growth of cratons by accretion. Finally, magmatic nickel deposits are mostly Archean and Proterozoic in
133 age and commonly occur on thick lithosphere (≥ 150 km). Unlike other base metal deposits, their distribution is
134 associated with edges of even thicker lithosphere (~ 200 km), broadly consistent with previous studies showing
135 major lithospheric structural controls on deposit locations.⁷ Their generation requires large fraction partial melting
136 of peridotite, indicative of high mantle temperatures (more prevalent in a early, hotter Earth) and decompression
137 melting at shallow depths.²⁷ Therefore, their present distribution suggests lithospheric thickness must have locally
138 increased since formation, simultaneously enhancing preservation potential.

139 In summary, this work illustrates a new and remarkably clear link between giant sediment-hosted base metal
140 mineral systems and the edges of thick lithosphere. Approximately 55% of the world's lead, 45% of its zinc and 20%
141 of known copper is found within ~ 200 km of this edge. We have demonstrated the value of regional seismic arrays to
142 better resolve this edge and enhance the mineral exploration efforts required to sustain ongoing global development.
143 Significantly, deposit ages indicate that, following rifting, edges of thick-lithosphere are generally stable over billion-
144 year timescales. The far-reaching geodynamic and societal implications of our observations highlight the urgent
145 need for further research. To improve resolution of mapped lithospheric structure, higher fidelity seismic imaging
146 must be coupled with enhanced mantle xenolith coverage and tighter constraints on seismic anelasticity from
147 mineral physics experiments. More generally, these maps need to be integrated with models of basin dynamics,
148 surface processes and reactive transport modelling, and bench-marked against additional geological information,
149 such as sedimentary facies variations, tectonic structures and alteration zones. These multiple research strands
150 will yield fundamental new insights into sediment-hosted mineral systems and lead to substantial improvements in
151 exploration success rates.

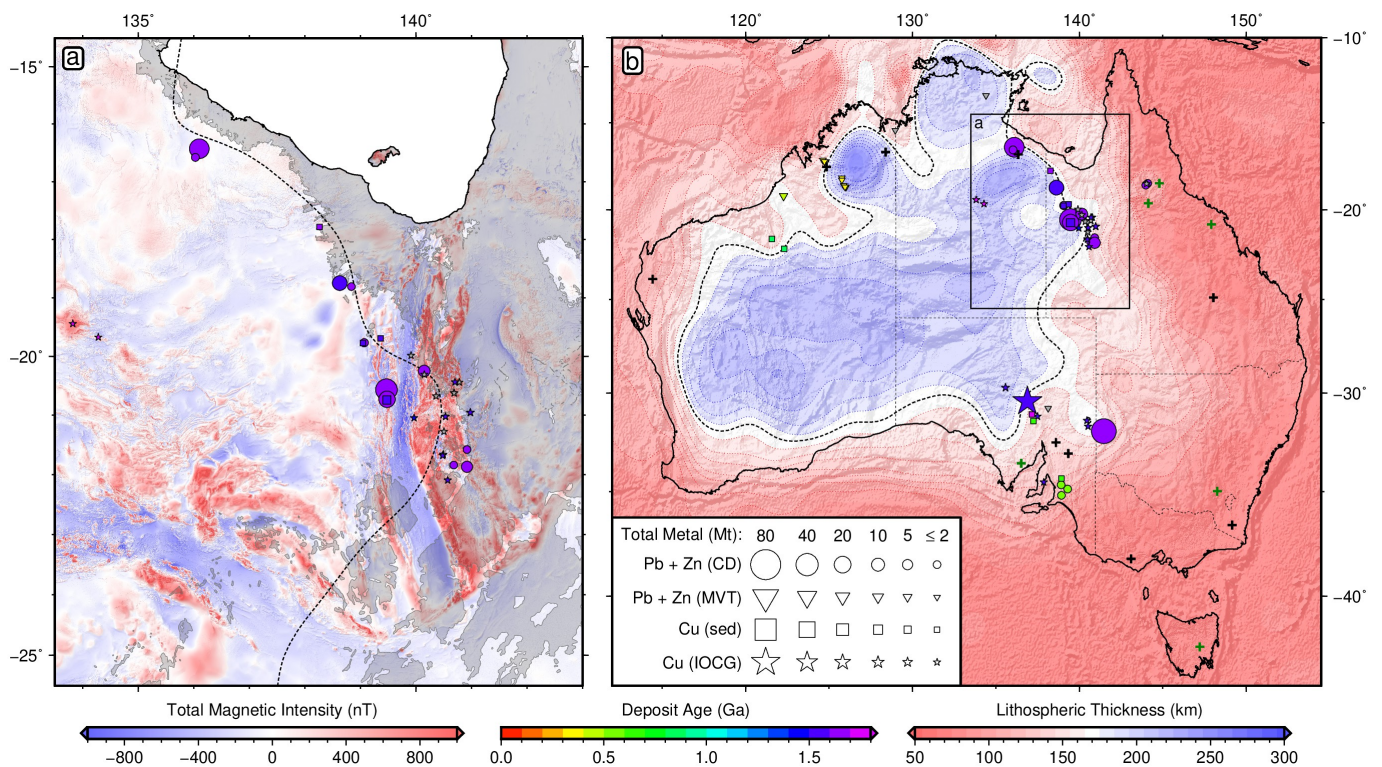


Figure 1: **Distribution of sediment-hosted and iron-oxide-copper-gold base metal deposits as a function of lithospheric thickness in Australia.** (a) Carpentaria Zinc Belt; red/blue = variably reduced to pole aeromagnetic intensity data¹³; grey polygons = generalised outcrop of Cretaceous marine sediments in Eromanga and Karumba Basins²⁸; black dashed contour = 170 km LAB thickness; symbols = deposit locations; area proportional to estimate of total contained mass of metal (Mt = megatonnes); unknown deposit size given 2 Mt symbol; colour = ore body formation age (billion years); unknown age plotted in grey; circles = clastic-dominated lead-zinc (PbZn-CD); triangles = Mississippi Valley type lead-zinc (PbZn-MVT); squares = sedimentary copper (Cu-sed); stars = iron-oxide-copper-gold (IOCG). (b) LAB mapped by converting FR12 tomography¹⁶ to temperature using an anelasticity parameterisation¹⁵ calibrated on local paleogeotherms (Supplementary Material) and illuminated by free-air gravity anomalies¹³; black/green crosses = geotherms used as constraints/tests in anelasticity calibration; box = location of panel (a).

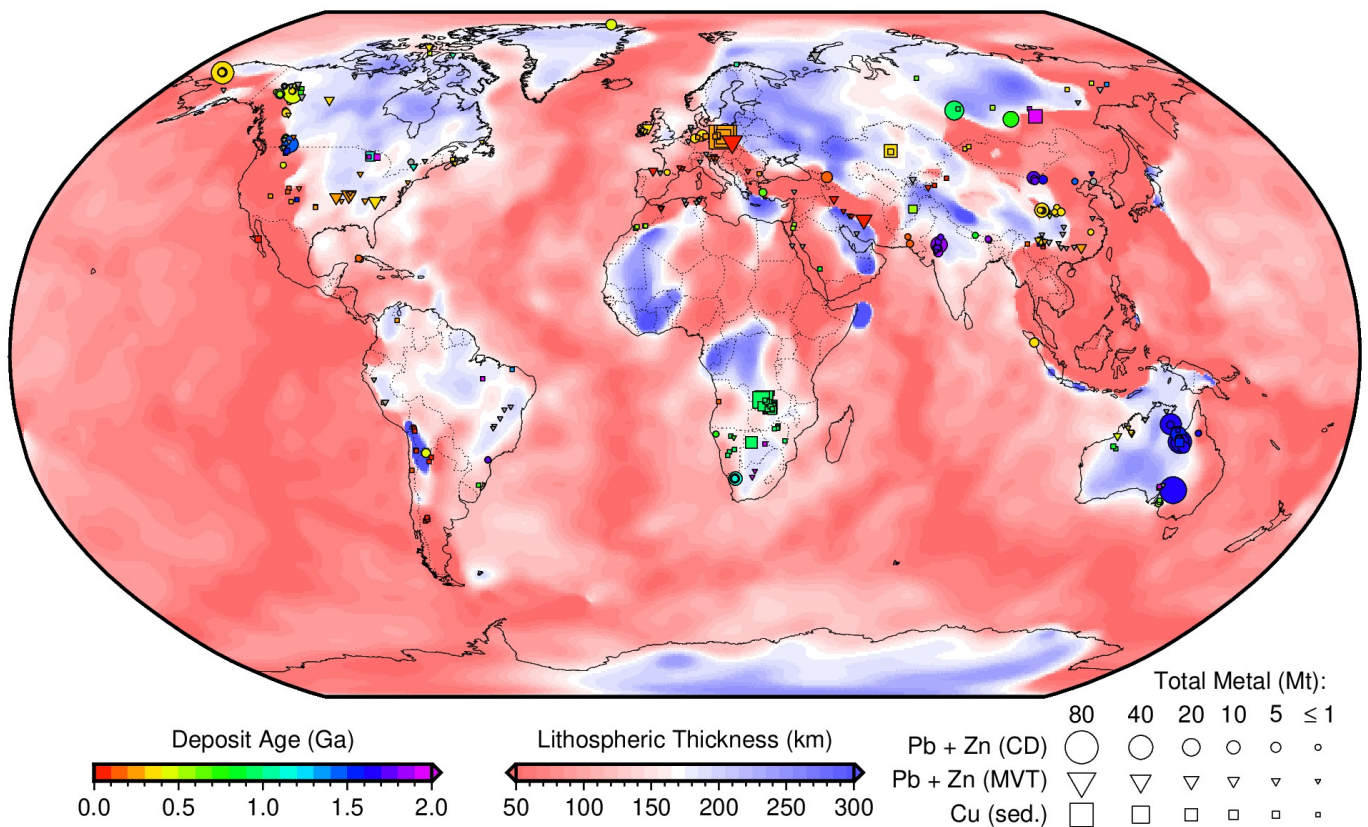


Figure 2: **Global distribution of sediment-hosted base metal deposits as a function of lithospheric thickness.** LAB derived from SL2013sv tomography model¹⁷ using a calibrated anelasticity parameterisation¹⁵ (Methods). Symbols = deposit locations; area proportional to estimate of total contained mass of metal (Mt = megatonnes); unknown deposit size given 1 Mt symbol; colour = ore body formation age (billion years); unknown age plotted in grey; circles = clastic-dominated lead-zinc (PbZn-CD); triangles = Mississippi Valley type lead-zinc (PbZn-MVT); squares = sedimentary copper (Cu-sed.).

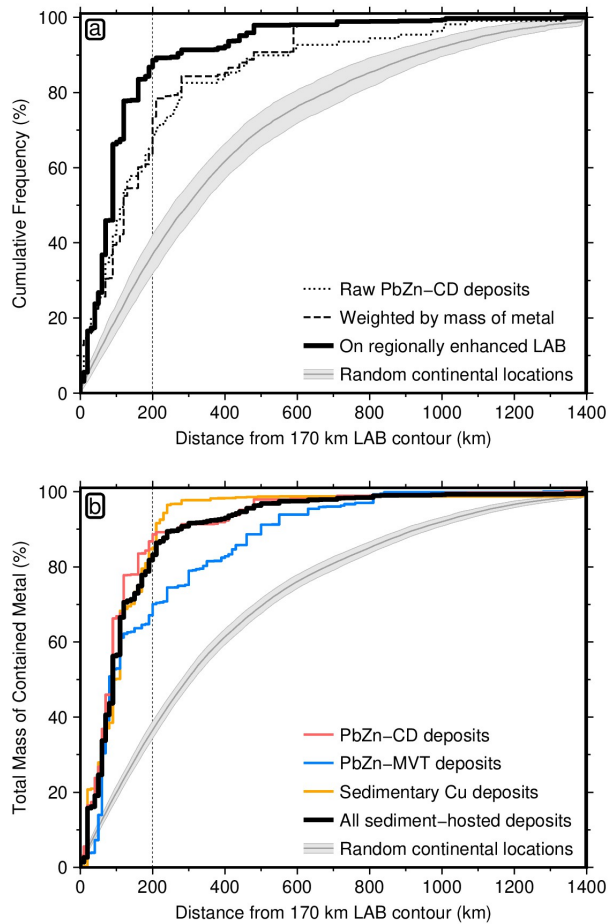


Figure 3: **Cumulative distribution functions for global sediment-hosted base metals.** (a) Different approaches for counting 109 clastic-dominated lead-zinc deposits (PbZn-CD). Dotted line = simple count of number of deposits with increasing distance from the 170 km contour in global LAB map (Figure 2); dashed line = weighting by contained mass of lead and zinc; solid black line = mass-weighted deposits where the Australian LAB has been replaced with the regionally enhanced map (Figure 1b); grey line/bounds = mean and standard deviation of 100 sets of equivalent number of randomly drawn continental locations, with respect to regionally enhanced LAB. (b) Weighted, regionally enhanced CDFs for 109 PbZn-CD, 147 Mississippi Valley-type (PbZn-MVT), 139 sedimentary copper (Cu-sed) and combination of all three. Grey band as before for combined database.

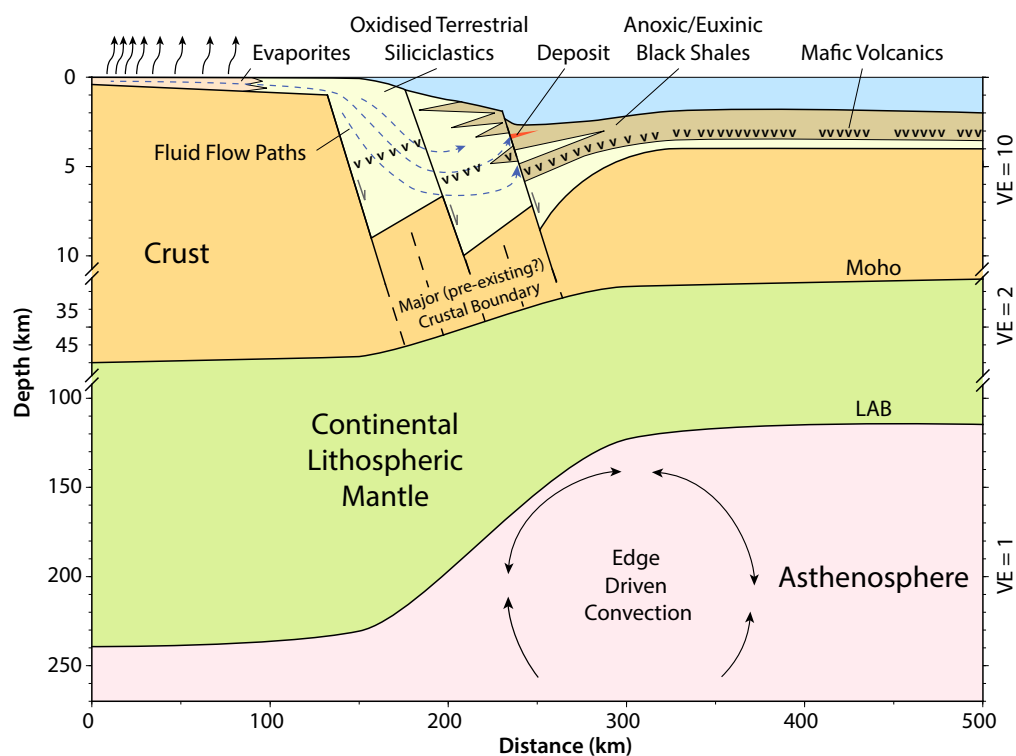


Figure 4: **Schematic illustration of sediment-hosted base metal deposit genesis in extensional settings.** Influence of lithospheric edge on mineral system components during rifting. Basinal brines sourced from evaporites scavenge metals from oxidised terrestrial sediments and volcanics (v) on route to metal deposition sites in black shales.²² Notice variable vertical exaggeration (VE) and prominence of the lithosphere-asthenosphere boundary edge illustrated at 1:1 scale. Schematic based on architectural constraints from the Australian Carpentaria Zinc Belt and Polish Fore-Sudetic Block.

152 Methods

153 **Deposit compilation.** Our global inventory of 2141 major base metal deposits are categorised into six classes.
154 Three are sediment hosted: sedimentary copper (Cu-sed); elastic-dominated lead-zinc (PbZn-CD); and Mississippi
155 Valley-type lead-zinc (PbZn-MVT). The other three are associated with magmatic systems: copper porphyry (Cu-
156 por); magmatic nickel-copper-platinum group elements (Ni-Cu-PGE); and volcanogenic massive sulfides (VMS). For
157 each deposit, we include the type (based on established classification schemes), location, age (direct measurement or
158 inferred based on geological relationships) and total resource size by combining historical production with estimated
159 resources. Our Cu-sed deposit dataset follows the classification scheme and compilation of Hitzman et al. (2005),
160 cross-checked against Cox et al. (2007).^{29,30} Where these two compilations disagree on deposit size, the larger
161 value has been used. Our PbZn-CD and PbZn-MVT deposit compilations extensively revise and build on the work
162 of Taylor et al. (2009).³¹ References for each deposit type were manually checked and additional references have
163 been included. We exploit the compilation of Sillitoe (2010) for Cu-por deposits.³² Our magmatic Ni-Cu-PGE
164 compilation follows Hoatson et al. (2006), with deposit location populated from disparate sources.³³ Our catalogue
165 of VMS deposits is an extensive revision of the compilation by Franklin et al. (2005).³⁴ Australian information for
166 all the above deposit types, with the addition of 25 iron-oxide-copper-gold deposits, was updated using the authors'
167 own knowledge, building on the Geoscience Australia OZMin database.³⁵ We have endeavoured to assemble the most
168 complete deposit dataset possible by revising and extending pre-existing compilations (Supplementary Information).
169 Importantly, patchy or absent reporting of mineral deposit information from some countries inevitably means our
170 global database is incomplete, but we do not believe that this will impact the veracity of our main conclusions.

171 **Choice of seismic tomography model.** Our LAB maps are based on the most recent, high-resolution shear
172 wave tomography models. For the global map, we use SL2013sv¹⁷ which is an upper mantle-only model built
173 from a combination of body and surface waves, including fundamental and higher modes. Periods considered are
174 11–450 s, ~ 750,000 seismograms are included, and misfits are calculated between synthetics and the full waveform
175 up to the 9th overtone. Crucially, simultaneous inversion for the crustal model results in minimal smearing of slow
176 crustal velocities down into the upper mantle, thereby allowing us to use more depth slices in our V_S to temperature
177 calibration. Checkerboard resolution tests indicate that features ~ 600 km in diameter at lithospheric depths are
178 generally well resolved. Finer features should be resolvable in regions with dense ray path coverage, such as North
179 America, Europe and southeast Asia. The SL2013sv model contains only 6 seismometers in Australia, so has limited
180 resolution within this continent. Therefore, we also investigate the FR12 regional seismic tomography model¹⁶ to
181 generate a high resolution map for the Australian continent. FR12 is a radially isotropic V_S model derived from
182 Rayleigh wave travel times.³⁶ Periods considered are 50–120 s and the fundamental and first four higher modes
183 have been used where possible, leading to good sensitivity down to ~ 250 km depths. It contains a greater number
184 of source–receiver paths (> 13,000) compared to other Australian models. However, it uses an *a priori* crustal
185 model that remains fixed throughout the inversion, resulting in noticeable smearing of crustal velocities into the
186 upper mantle. Checkerboard tests indicate that features ~ 300 km in diameter at lithospheric depths are well
187 resolved.

188 **Parameterising shear-wave anelasticity.** For converting shear-wave velocities (V_S) to temperature, we
 189 adopt the parameterisation of Yamauchi & Takei (2016)¹⁵, which includes effects of anelasticity in pre-melt condi-
 190 tions (temperatures above $\sim 90\%$ of melting temperature). V_S is defined as

$$191 \quad V_S = \frac{1}{\sqrt{\rho J_1}} \left(\frac{1 + \sqrt{1 + (J_2/J_1)^2}}{2} \right)^{-\frac{1}{2}} \simeq \frac{1}{\sqrt{\rho J_1}} \quad (1)$$

192 where ρ is the density and J_1 and J_2 represent real and imaginary components of the complex compliance, J^* ,
 193 which is a quantity describing the sinusoidal strain resulting from the application of a unit sinusoidal stress. J_1
 194 represents the strain amplitude in phase with the driving stress, whilst the J_2 component is $\frac{\pi}{2}$ out of phase, resulting
 195 in dissipation. These terms are expressed as

$$196 \quad J_1(\tau'_S) = J_U \left[1 + \frac{A_B [\tau'_S]^{\alpha_B}}{\alpha_B} + \frac{\sqrt{2\pi}}{2} A_P \sigma_P \left\{ 1 - \operatorname{erf} \left(\frac{\ln[\tau'_P/\tau'_S]}{\sqrt{2}\sigma_P} \right) \right\} \right] \quad (2)$$

$$197 \quad J_2(\tau'_S) = J_U \frac{\pi}{2} \left[A_B [\tau'_S]^{\alpha_B} + A_P \exp \left(-\frac{\ln^2[\tau'_P/\tau'_S]}{2\sigma_P^2} \right) \right] + J_U \tau'_S \quad (3)$$

199 where $A_B = 0.664$ and $\alpha_B = 0.38$ represent the amplitude and slope of background stress relaxation and J_U is the
 200 unrelaxed compliance. Parameters A_P and σ_P represent the amplitude and width of a high frequency relaxation
 201 peak superimposed on this background trend such that

$$202 \quad A_P(T') = \begin{cases} 0.01 & \text{for } T' < 0.91 \\ 0.01 + 0.4(T' - 0.91) & \text{for } 0.91 \leq T' < 0.96 \\ 0.03 & \text{for } 0.96 \leq T' < 1 \\ 0.03 + \beta(\phi_m) & \text{for } T' \geq 1 \end{cases} \quad (4)$$

203 and

$$204 \quad \sigma_P(T') = \begin{cases} 4 & \text{for } T' < 0.92 \\ 4 + 37.5(T' - 0.92) & \text{for } 0.92 \leq T' < 1 \\ 7 & \text{for } T' \geq 1 \end{cases} \quad (5)$$

205 where T' is homologous temperature ($\frac{T}{T_s}$) with T the temperature and T_s the solidus temperature, both in Kelvin.
 206 ϕ_m is the melt fraction and $\beta(\phi_m)$ describes the direct poroelastic effect of melt (assumed to be negligible under
 207 upper mantle conditions). For this case, J_U is the inverse of the unrelaxed shear modulus, $\mu_U(P, T)$, such that

$$208 \quad J_U(P, T)^{-1} = \mu_U(P, T) = \mu_U^0 + \frac{\partial \mu_U}{\partial T} (T - T_0) + \frac{\partial \mu_U}{\partial P} (P - P_0) \quad (6)$$

209 where μ_U^0 is the unrelaxed shear modulus at surface pressure-temperature conditions, the differential terms are
 210 assumed to be constant and the pressure, P , in GPa is linearly related to the depth, z , in km by $\frac{z}{30}$. The
 211 normalised shear wave period, τ'_S , in Equations (2) and (3) is equal to $\frac{\tau_S}{2\pi\tau_M}$, where τ_S is the shear wave period

212 and $\tau_M = \frac{\eta}{\mu_U}$ is the normalised Maxwell relaxation timescale. τ'_P represents the normalised shear-wave period
 213 associated with the centre of the high frequency relaxation peak, assumed to be 6×10^{-5} . The shear viscosity, η , is

$$214 \quad \eta = \eta_r \left(\frac{d}{d_r} \right)^m \exp \left[\frac{E_a}{R} \left(\frac{1}{T} - \frac{1}{T_r} \right) \right] \exp \left[\frac{V_a}{R} \left(\frac{P}{T} - \frac{P_r}{T_r} \right) \right] A_\eta \quad (7)$$

215 where d is the grain size, m the grain size exponent (assumed to be 3), R the gas constant, E_a the activation
 216 energy and V_a the activation volume. Subscripts $[X]_r$ refer to reference values, assumed to be $d_r = d = 1$ mm,
 217 $P_r = 1.5$ GPa and $T_r = 1200^\circ\text{C}$ for the upper mantle. A_η represents the extra reduction of viscosity due to an
 218 increase in E_a near the solidus, expressed as

$$219 \quad A_\eta(T') = \begin{cases} 1 & \text{for } T' < T'_\eta \\ \exp \left[-\frac{(T' - T'_\eta)}{(T' - T'_\eta T'_\eta)} \ln(\gamma) \right] & \text{for } T'_\eta \leq T' < 1 \\ \gamma^{-1} \exp(\lambda\phi) & \text{for } T' \geq 1 \end{cases} \quad (8)$$

220 where T'_η is the homologous temperature above which activation energy becomes $E_a + \Delta E_a$ and $\gamma = 5$ is the factor
 221 of additional reduction. $\lambda\phi$ describes the direct effect of melt on viscosity, assumed to be negligible here. The
 222 solidus temperature, T_s , is fixed to a value of 1326°C at 50 km equivalent to a dry peridotite solidus³⁷ and linearly
 223 increases below this depth according to

$$224 \quad T_s(z) = 1599 + \frac{\partial T_s}{\partial z}(z - 50 \text{ km}) \quad (9)$$

225 where $\frac{\partial T_s}{\partial z}$ is the solidus gradient. We use a temperature-dependent, compressible density, $\rho(P, T)$, following the
 226 approach of Grose & Afonso (2013).³⁸ First, we define a linear temperature-dependence on thermal expansivity,
 227 $\alpha(T)$, such that

$$228 \quad \alpha(T) = \alpha_0 + \alpha_1 T \quad (10)$$

229 where $\alpha_0 = 2.832 \times 10^{-5} \text{ }^\circ\text{C}^{-1}$ and $\alpha_1 = 0.758 \times 10^{-8} \text{ }^\circ\text{C}^{-2}$ are constants calibrated from mineral physics
 230 experiments. To include pressure-dependence, the isothermal volume change, $(V_0/V)_T$ is calculated at each pressure
 231 using a Brent minimisation algorithm and the third-order Birch-Murnaghan equation of state

$$232 \quad P = \frac{3}{2} K_0 \left[\left(\frac{V_0}{V} \right)_T^{\frac{7}{3}} - \left(\frac{V_0}{V} \right)_T^{\frac{5}{3}} \right] \left\{ 1 + \frac{3}{4} (K'_T - 4) \left[\left(\frac{V_0}{V} \right)_T^{\frac{2}{3}} - 1 \right] \right\} \quad (11)$$

233 where $K_0 = 130$ GPa is the bulk modulus at zero pressure and $K'_T = 4.8$ is the pressure-derivative of the isothermal
 234 bulk modulus. The associated isothermal density change with pressure, $\rho(P)$, is given by

$$235 \quad \rho(P) = \rho_0 \left(\frac{V_0}{V} \right)_T \quad (12)$$

236 where $\rho_0 = 3.33 \text{ Mg m}^{-3}$ is the density of mantle at surface pressure and temperature. The effect of pressure on

237 thermal expansivity is included according to

$$238 \quad \frac{\alpha(P, T)}{\alpha(T)} = \left(\frac{V_0}{V}\right)_T \exp \left\{ (\delta_T + 1) \left[\left(\frac{V_0}{V}\right)_T^{-1} - 1 \right] \right\} \quad (13)$$

239 where $\delta_T = 6$ is the Anderson-Grüneisen parameter. Thus, the final density, $\rho(P, T)$, can be calculated using

$$240 \quad \rho(P, T) = \rho_0 \left(\frac{V_0}{V}\right)_T \left\{ 1 - \left[\frac{\alpha(P, T)}{\alpha(T)} \right] \left[\alpha_0(T - T_0) + \frac{\alpha_1}{2}(T^2 - T_0^2) \right] \right\} \quad (14)$$

241 where $T_0 = 273$ K is temperature at the surface. In a similar manner to Equation (1), the shear-wave attenuation, Q_S^{-1} , can be defined as

$$243 \quad Q_S^{-1} = \frac{J_2}{J_1} \left(\frac{1 + \sqrt{1 + (J_2/J_1)^2}}{2} \right)^{-1} \simeq \frac{J_2}{J_1} \quad (15)$$

244 **Xenolith and xenocryst thermobarometry.** Temperature estimates across a range of depths are required
 245 to generate a series of V_S -T-P tie points in order to calibrate the regional seismic tomography models. We therefore
 246 assemble a suite of fifteen Australian paleogeotherms derived from thermobarometric analysis of mantle xenoliths
 247 and xenocrysts (Supplementary Information). These come from a range of settings between thick and thin litho-
 248 sphere. Localities with thin lithosphere tend to have data obtained from whole xenolith samples, typically hosted
 249 in basaltic volcanic products. For these cases, the compositions of multiple phases (garnet, clinopyroxene, orthopy-
 250 roxene and olivine) can be obtained that all equilibrated under the same pressure-temperature (P-T) conditions.
 251 In these samples, we use a thermometer³⁹ that exploits exchange of calcium and magnesium between orthopy-
 252 roxene and clinopyroxene and a barometer⁴⁰ based upon aluminium exchange between orthopyroxene and garnet,
 253 given by equation (5) of Nickel & Green (1985). This approach therefore requires compositions of garnet, diopside
 254 (clinopyroxene) and enstatite (orthopyroxene) for each xenolith. This barometer and thermometer pair both also
 255 depend upon the temperature and pressure, respectively. These two equations are therefore solved simultaneously
 256 by iteration to obtain equilibration P-T conditions. Samples are discarded if they fail more than one of the eight
 257 oxide, cation and equilibration checks.⁴¹ Analyses from locations on thicker lithosphere are predominantly obtained
 258 from heavy mineral concentrates generated during diamond exploration (plus rare diamond inclusions and occa-
 259 sional whole peridotite xenoliths), where the association of one mineral grain with any other has been lost. Thus,
 260 the approach outlined above using multiple phases is unavailable, and we instead turn to single grain combined
 261 thermobarometers for deriving equilibration P-T conditions. For these samples, we use the chrome-in-diopside
 262 barometer⁴² that exploits the exchange of chromium between clinopyroxene and garnet (Equation (9) of Nimis &
 263 Taylor, 2000). It uses only diopside compositions, but requires that garnet was also present in the source region.
 264 The associated thermometer⁴² exploits enstatite-in-diopside, again using only diopside compositions but requiring
 265 that orthopyroxene was present within the source. The temperature is given by Equation (17) of Nimis & Taylor
 266 (2000). Again, these two equations must be solved by iteration to obtain P-T conditions for each diopside grain.
 267 Calibration on laboratory experiments has shown that this thermobarometer may become inaccurate at low pres-
 268 sures and at temperatures $<700^\circ\text{C}$.⁴¹ We therefore only use P-T estimates derived from this thermobarometer that
 269 yield depths >60 km and pass both of the clinopyroxene cation and oxide checks.

270 **Fitting a geotherm to P-T estimates.** For each locality, P-T estimates derived from thermobarometry
 271 are entered into FITPLOT^{43,44} to constrain the best-fitting paleogeotherm (Supplementary Information). Within
 272 the crust, we adopt a constant conductivity of 2.5 W m⁻¹ °C⁻¹, whilst a pressure- and temperature-dependent
 273 parameterisation⁴⁵ is used within the mantle. Radiogenic heat production is assumed to be 1.12 μW m⁻³ in the
 274 upper crust, 0.40 μW m⁻³ in the lower crust and zero within the mantle.⁴⁶ Crustal thickness at each location is
 275 obtained from the AusMoho model⁴⁷, with upper and lower crustal layers assigned equal thicknesses. We assume
 276 a potential temperature of 1333°C, which is the temperature required to match the thickness and geochemistry of
 277 mid-ocean ridge basalt from a dry lherzolite source using a corner-flow melting parameterisation.^{48,49} Self-consistent
 278 parameters are used to calculate the adiabatic gradient, including a reference density of $\rho_0 = 3.3 \text{ Mg m}^{-3}$, thermal
 279 expansivity of $\alpha = 3 \times 10^{-5} \text{ °C}^{-1}$ and specific heat capacity of $C_P = 1187 \text{ J kg}^{-1} \text{ °C}^{-1}$.

280 **Calibrating V_S to temperature conversion.** Anelasticity parameters A_B , α_B , τ'_P , $\beta(\phi_m)$, γ , T'_η and $\lambda\phi$
 281 have been directly constrained by forced oscillation experiments on borneol.¹⁵ However, μ_U^0 , $\frac{\partial\mu_U}{\partial T}$, $\frac{\partial\mu_U}{\partial P}$, η_r , E_a , V_a
 282 and $T_S(z)$ must be independently determined by inverting real-Earth observational constraints on temperature,
 283 shear-wave velocity, attenuation and viscosity. Therefore, the SL2013sv global V_S model¹⁷ is stacked in oceanic
 284 regions to calculate average V_S as a function of depth and lithospheric age. The age grid and optimal thermal
 285 model for a cooling oceanic plate are adopted from Richards et al. (2018).¹⁸ At each depth slice of the tomography
 286 model, a suite of V_S versus temperature tie-points are extracted. Misfit, H_1 , between predicted and observed V_S is

$$H_1 = \sqrt{\frac{1}{N} \sum_{i=1}^N \frac{1}{M} \sum_{j=1}^M \left(\frac{V_{ij}^o - V_{ij}^c}{\sigma_{ij}} \right)^2} \quad (16)$$

288 where V_{ij}^o are observed shear-wave velocities with associated standard deviation σ_{ij} , V_{ij}^c is the prediction from
 289 Equation (1), M is the number of age bins at a given depth and N is the number of depth slices. A second
 290 suite of tie-points is created by assuming that temperatures are isentropic at depths well below the upper thermal
 291 boundary layer. We calculate average V_S as a function of depth over oceanic regions in the global model, and
 292 over the whole spatial domain in regional models. Over the depth range 250–400 km, beyond which the resolving
 293 power of surface waves drops significantly, these values are combined with an isentrope calculated for pyrolite with
 294 a potential temperature of 1334 °C using *Perple-X*. Misfit for the isentrope, H_2 , is

$$H_2 = \sqrt{\frac{1}{N} \sum_{i=1}^N \left(\frac{V_i^o - V_i^c}{\sigma_i} \right)^2} \quad (17)$$

296 It has been observed that over the depth range 150–400 km, both V_S and Q_S^{-1} are relatively consistent for oceanic
 297 ages ≥ 100 Ma. Over this range, we stack the QRFS12 attenuation model⁵⁰, generating a suite of Q_S^{-1} to V_S
 298 tie-points as a function of depth. Equations (1) and (15) are coupled such that average temperature is obtained
 299 from the average V_S , rather than assuming isentropic temperatures extend up to 150 km. Misfit, H_3 , between

300 observed and predicted attenuation is

$$H_3 = \sqrt{\frac{1}{N} \sum_{i=1}^N \left(\frac{Q_i^{-1} o - Q_i^{-1} c}{\sigma_i^*} \right)^2} \quad (18)$$

302 We also adopt the bulk viscosity measurement⁵¹ of $\eta_{ref} = 3 \times 10^{20}$ Pa s for upper mantle (~ 100 –670 km) and
 303 compare it to the mean predicted value for 225–400 km depths obtained from Equation (7). Misfit, H_4 , is calculated
 304 using

$$H_4 = \sqrt{\left(\left\{ \frac{1}{N} \sum_{i=1}^N \log_{10} [\eta_i^c] \right\} - \log_{10} [\eta_{ref}] \right)^2} \quad (19)$$

306 where η_i^c is predicted viscosity. Finally, for calibration of regional tomography models, we take the better con-
 307 strained paleogeotherms derived from thermobarometry on mantle xenoliths. Argyle, Boowinda Creek, Bullenmerri,
 308 Ellendale, Merline, Monaro, Monk Hill, Orroroo and Wandagee are used to constrain each anelasticity model. None
 309 of these paleogeotherms show evidence of having been perturbed by heating events immediately prior to xenolith
 310 entrainment therefore the calculated PT conditions are taken to indicate ambient mantle conditions at entrainment.
 311 Less well constrained paleogeotherms from Bow Hill, Cleve, Cone 32, Jugiong, Mt St Martin and Sapphire Hill are
 312 used to visually check results. For each utilised paleogeotherm we extract temperatures every 5 km between the
 313 base of the thermal boundary layer and either 125 km for regions with thick lithosphere, or 50 km for those with
 314 thin (<100 km) lithosphere. These variable top depths minimise the impact of potential crustal bleeding artefacts.
 315 Extracting $V_S(z)$ values at each paleogeotherm location yields a suite of V_S to temperature tie-points. Misfit, H_5 ,
 316 is calculated from

$$H_5 = \sqrt{\frac{1}{N} \sum_{i=1}^N \frac{1}{M} \sum_{j=1}^M \left(\frac{V_{ij}^o - V_{ij}^c}{\sigma_{ij}} \right)^2} \quad (20)$$

318 where M is the number of paleogeotherms, N is the number of tie-points associated with each geotherm and σ_{ij}
 319 reflects uncertainty in the V_S measurement, assumed to be a constant 0.1 km s^{-1} which captures typical variations
 320 between different tomography models at a given location. Combined misfit, H , is given by

$$H = \frac{w_1 H_1 + w_2 H_2 + w_3 H_3 + w_4 H_4 + w_5 H_5}{w_1 + w_2 + w_3 + w_4 + w_5} \quad (21)$$

322 where w represents weighting applied to each misfit constraint. H is minimised in two steps. Initially, a pa-
 323 rameter sweep is performed to identify the approximate location of the global minimum. μ_U^0 is varied between
 324 69–82 GPa (in increments of 1 GPa), $\frac{\partial \mu}{\partial T}$ between -20 and $-8 \text{ MPa } ^\circ\text{C}^{-1}$ ($2 \text{ MPa } ^\circ\text{C}^{-1}$ increments), $\frac{\partial \mu}{\partial T}$ be-
 325 tween 1.5–2.9 (0.2 increments), η_r between 10^{17} – 10^{23} Pa s ($10^{0.5}$ Pa s increments), E_a between 100–1000 kJ mol^{-1}
 326 (100 kJ mol^{-1} increments), V_a between 0–30 $\text{cm}^3 \text{ mol}^{-1}$ ($2 \text{ cm}^3 \text{ mol}^{-1}$ increments) and $\frac{\partial T_s}{\partial z}$ between 0–4.5 $^\circ\text{C km}^{-1}$
 327 ($0.25 \text{ } ^\circ\text{C km}^{-1}$ increments), in line with ranges of previous estimates obtained from laboratory experiments and
 328 other studies.^{14,15,52} Secondly, Powell’s conjugate gradient algorithm is used to further minimise H using best-
 329 fitting parameters from the initial sweep as the starting point. For calibration of the global model SL2013sv, we
 330 set $w_1 = 10$, $w_2 = 1$, $w_3 = 2$, $w_4 = 2$ and $w_5 = 0$, which yields a minimum misfit $H = 0.682$ when $\mu_U^0 = 76.3$ GPa,

331 $\frac{\partial \mu_U}{\partial T} = -17.7 \text{ MPa } ^\circ\text{C}^{-1}$, $\frac{\partial \mu_U}{\partial P} = 2.53$, $\eta_r = 1.23 \times 10^{21} \text{ Pa s}$, $E_a = 202 \text{ kJ mol}^{-1}$, $V_a = 1.92 \text{ cm}^3 \text{ mol}^{-1}$ and
332 $\frac{\partial T_s}{\partial z} = 0.955 \text{ }^\circ\text{C km}^{-1}$. These parameters are used to convert the full three-dimensional V_S model to temperature.
333 For the regional model FR12 we constrain the calibration using the paleogeotherms. All weights are set to zero
334 except for $w_2 = 1$ and $w_5 = 10$, yielding minimum misfit $H = 0.578$ when $\mu_U^0 = 69.3 \text{ GPa}$, $\frac{\partial \mu_U}{\partial T} = -12.3 \text{ MPa } ^\circ\text{C}^{-1}$,
335 $\frac{\partial \mu_U}{\partial P} = 2.89$, $\eta_r = 1.93 \times 10^{22} \text{ Pa s}$, $E_a = 1000 \text{ kJ mol}^{-1}$, $V_a = 0 \text{ cm}^3 \text{ mol}^{-1}$ and $\frac{\partial T_s}{\partial z} = 4.50 \text{ }^\circ\text{C km}^{-1}$.

336 **Mapping the lithosphere-asthenosphere boundary.** A recent study¹⁸ on the thermal structure of oceanic
337 lithosphere found that the $1175 \pm 50^\circ\text{C}$ isotherm provides a good match to seismological observations of the
338 lithosphere-asthenosphere boundary (LAB), such as peak variation in the orientation of azimuthal anisotropy. In
339 this study, we therefore adopt this isotherm as a proxy for lithospheric thickness beneath the continents. $T(z)$ is
340 extracted from the V_S model and $\frac{\partial T}{\partial z}$ calculated over 25 km increments. Starting from the surface and progressing
341 downwards, when temperature passes the 1175°C threshold, LAB depth is calculated using linear interpolation,
342 with one important exception. In locations of thick crust, low V_S values at shallow depths arising from crustal
343 bleeding are erroneously interpreted as hot lithospheric mantle. In the regional seismic tomography models, this
344 crustal bleeding can be observed down to $\sim 125 \text{ km}$ in some locations (Figure S7). Therefore, when an inverted
345 temperature gradient is found at shallow depths, we move on to deeper levels until temperature starts to increase
346 with depth. This crustal bleeding is only considered down to 200 km. Maximum LAB depth is limited to 350 km or
347 the deepest slice in the seismic tomography model. Our 1175°C isotherm LAB proxy is shallower than used in some
348 other studies^{44,14} that define the LAB using the intersection of conductive and adiabatic temperature gradients in
349 the thermal boundary layer (typically occurring at temperatures $1350\text{--}1450^\circ\text{C}$). However, in addition to matching
350 oceanic observations, the 1175°C isotherm corresponds to lower homologous temperatures, where uncertainty in
351 anelasticity parameters has a smaller impact on the recovered LAB.

352 **Test suites of random continental locations.** In order to test the statistical significance of real deposit
353 locations, a test suite of random points on a sphere have been generated by randomly selecting two variables, a
354 and b , in the range 0–1 and converting into longitude, θ , and latitude, ϕ , using area-normalised relationships

$$355 \quad \theta = 360 \times a \quad (22)$$

$$356 \quad \phi = \frac{180}{\pi} \times \arcsin(2b - 1) \quad (23)$$

358 These are subsequently filtered to select only those points that lie onshore (Supplementary Information). For each
359 location, the closest approach of the 170 km lithospheric thickness contour is calculated and the resulting distances
360 are plotted in a cumulative distribution function (CDF).

361 **Kolmogorov-Smirnov statistical tests.** We use the *two-sample Kolmogorov-Smirnov test* to examine
362 whether the difference between two cumulative distribution functions is significant, given their respective pop-
363 ulation sizes. The D-value is the maximum magnitude of the difference between two CDFs at any point.²⁰ The
364 test calculates the probability that a D-value of this magnitude might accidentally occur, had the two CDFs been

365 randomly selected from the same underlying population. The probability, P , is approximated using

$$366 \quad P \approx \exp\left(\frac{-2pqD^2}{p+q}\right) \quad (24)$$

367 where p and q are the number of samples in each CDF and D is the D-value expressed as a fraction between 0
368 and 1. For each Kolmogorov-Smirnov test, a number of random points are generated that is equivalent to the
369 number of real deposits of that type (109 for PbZn-CD, 147 for PbZn-MVT and 139 for sedimentary copper).
370 Given the low sample size for some of the deposit classes, the distribution of this random set can vary somewhat
371 from the true average distribution of random continental locations. We therefore draw a test set in this manner 100
372 times and report the Kolmogorov-Smirnov statistics associated with each separate test within a histogram. The
373 D-value between the real non-weighted, regionally enhanced PbZn-CD CDF and each random CDF is individually
374 calculated, yielding a mean and standard deviation of 0.36 ± 0.04 with extremes of 0.27–0.45. The equivalent values
375 are 0.27 ± 0.02 with extremes of 0.23–0.32 for the combined sediment-hosted deposits in Figure 2. A D-value of 0.27
376 for the 395 combined sedimentary-hosted deposits suggests that the probability this CDF is drawn from randomly
377 distributed continental points is less than 1 in 10^{12} (Supplementary Information).

378 References

- 379 [1] Ali, S. H. *et al.* Mineral supply for sustainable development requires resource governance. *Nature* **543**, 367–372
380 (2017).
- 381 [2] Schodde, R. Long term trends in global exploration – are we finding enough metal? In *11th*
382 *Fennoscandian Exploration and Mining Conference, 31st October 2017* (Levi, Finland, 2017). URL
383 minexconsulting.com/publications/oct2017b.
- 384 [3] Nassar, N. T., Graedel, T. E. & Harper, E. M. By-product metals are technologically essential but have
385 problematic supply. *Science Advances* **1**, 1–11 (2015).
- 386 [4] McCuaig, T. C., Beresford, S. & Hronsky, J. Translating the mineral systems approach into an effective
387 exploration targeting system. *Ore Geology Reviews* **38**, 128–138 (2010).
- 388 [5] Wyborn, L. A. I., Heinrich, C. A. & Jaques, A. L. Australian Proterozoic mineral systems: essential ingredients
389 and mappable criteria. *Australian Institute of Mining and Metallurgy Annual Conference* 109–115 (1994).
- 390 [6] McCuaig, T. C. & Hronsky, J. M. A. The mineral system concept: The key to exploration targeting. In
391 *Society of Economic Geologists Special Publication 18*, 153–175 (Society of Economic Geologists, 2014).
- 392 [7] Begg, G. C. *et al.* Lithospheric, cratonic, and geodynamic setting of Ni-Cu-PGE sulfide deposits. *Economic*
393 *Geology* **105**, 1057–1070 (2010).
- 394 [8] Griffin, W. L., Begg, G. C. & O'Reilly, S. Y. Continental-root control on the genesis of magmatic ore deposits.
395 *Nature Geoscience* **6**, 905–910 (2013).

- 396 [9] Leach, D. L. *et al.* Sediment-hosted lead-zinc deposits in Earth history. *Economic Geology* **105**, 593–625
397 (2010).
- 398 [10] Hitzman, M. W., Selley, D. & Bull, S. Formation of sedimentary rock-hosted stratiform copper deposits
399 through Earth history. *Economic Geology* **105**, 627–639 (2010).
- 400 [11] Huston, D. L. *et al.* Tectono-metallogenic systems – The place of mineral systems within tectonic evolution,
401 with an emphasis on Australian examples. *Ore Geology Reviews* **76**, 168–210 (2016).
- 402 [12] McCuaig, T. C., Scarselli, S., O’Connor, T., Busuttill, S. & N, M. The Power of a Systems Approach to Mineral
403 and Petroleum Exploration in Sedimentary Basins. *SEG Special Publication* **21** (2018).
- 404 [13] Geophysical Archive Data Delivery System (GADDS) (2018). URL geoscience.gov.au/gadds.
- 405 [14] Priestley, K. & McKenzie, D. P. The relationship between shear wave velocity, temperature, attenuation and
406 viscosity in the shallow part of the mantle. *Earth and Planetary Science Letters* **381**, 78–91 (2013).
- 407 [15] Yamauchi, H. & Takei, Y. Polycrystal anelasticity at near-solidus temperatures. *Journal of Geophysical*
408 *Research: Solid Earth* **121**, 7790–7820 (2016).
- 409 [16] Fishwick, S. & Rawlinson, N. 3-D structure of the Australian lithosphere from evolving seismic datasets.
410 *Australian Journal of Earth Sciences* **59**, 809–826 (2012).
- 411 [17] Schaeffer, A. J. & Lebedev, S. Global shear speed structure of the upper mantle and transition zone. *Geo-*
412 *physical Journal International* **194**, 417–449 (2013).
- 413 [18] Richards, F. D., Hoggard, M. J., Cowton, L. R. & White, N. J. Reassessing the thermal structure of oceanic
414 lithosphere with revised global inventories of basement depths and heat flow measurements. *Journal of Geo-*
415 *physical Research: Solid Earth* **123**, 9136–9161 (2018).
- 416 [19] Huston, D. L. & Champion, D. C. Spatial variations in lead isotope ratios from the Mount Isa–McArthur
417 mineral province, northeast Australia: Evidence for a cryptic crustal margin controlling the distribution of
418 world-class sediment-hosted zinc-lead-silver deposits .
- 419 [20] Kolmogorov, A. N. Sulla determinazione empirica di una legge di distribuzione. *Giornale dell’Istituto Italiano*
420 *degli Attuari* **4**, 83–91 (1933).
- 421 [21] Menzies, M., Xu, Y., Zhang, H. & Fan, W. Integration of geology, geophysics and geochemistry: A key to
422 understanding the North China Craton. *Lithos* **96**, 1–21 (2007).
- 423 [22] Manning, A. H. & Emsbo, P. Testing the potential role of brine reflux in the formation of sedimentary
424 exhalative (sedex) ore deposits. *Ore Geology Reviews* **102**, 862–874 (2018).
- 425 [23] Sloan, R. A., Jackson, J. A., McKenzie, D. P. & Priestley, K. Earthquake depth distributions in central Asia,
426 and their relations with lithosphere thickness, shortening and extension. *Geophysical Journal International*
427 **185**, 1–29 (2011).

- 428 [24] Gibson, G. *et al.* Basin architecture and evolution in the Mount Isa mineral province, northern Australia:
429 Constraints from deep seismic reflection profiling and implications for ore genesis. *Ore Geology Reviews* **76**,
430 414 – 441 (2016). URL <http://www.sciencedirect.com/science/article/pii/S0169136815002036>.
- 431 [25] Davies, D. R. & Rawlinson, N. On the origin of recent intraplate volcanism in Australia. *Geology* **42**, 1031–1034
432 (2014).
- 433 [26] Huston, D. L., Pehrsson, S., Eglington, B. M. & Zaw, K. The geology and metallogeny of volcanic-hosted
434 massive sulfide deposits: Variations through geologic time and with tectonic setting. *Economic Geology* **105**,
435 571–591 (2010).
- 436 [27] Arndt, N. T., Leshner, C. M. & Czamanske, G. K. Mantle-derived magmas and magmatic Ni-Cu-(PGE)
437 deposits. *Economic Geology 100th Anniversary Volume* 5–24 (2005).
- 438 [28] Raymond, O. Australian Geological Provinces 2018.01 edition. *Geoscience Australia Dataset eCat Id: 1*
439 (2018). URL ecat.ga.gov.au/geonetwork.
- 440 [29] Hitzman, M. W., Kirkham, R., Broughton, D., Thorson, J. & Selley, D. The sediment-hosted stratiform
441 Copper ore system. *Economic Geology 100th Anniversary Volume* (2005).
- 442 [30] Cox, D. P., Lindsey, D. A., Singer, D. A., Moring, B. C. & Diggles, M. F. Sediment-hosted copper deposits of
443 the world: Deposit models and database. *U.S. Geological Survey Open-File Report* (2007).
- 444 [31] Taylor, R. D., Leach, D. L., Bradley, D. C. & Pisarevsky, S. A. Compilation of mineral resource data for
445 Mississippi Valley-type and clastic-dominated sediment-hosted lead-zinc deposits. *U.S. Geological Survey*
446 *Open-File Report* **1297** (2009).
- 447 [32] Sillitoe, R. H. Porphyry copper systems. *Economic Geology* **105**, 3–41 (2010).
- 448 [33] Hoatson, D. M., Jaireth, S. & Jaques, A. L. Nickel sulfide deposits in Australia: Characteristics, resources,
449 and potential. *Ore Geology Reviews* **29**, 177–241 (2006).
- 450 [34] Franklin, J. M., Gibson, H. L., Jonasson, I. R. & Galley, A. G. Volcanogenic massive sulfide deposits. *Economic*
451 *Geology 100th Anniversary Volume* (2005).
- 452 [35] Sexton, J. Australian mineral occurrences collection. *Geoscience Australia Dataset eCat Id 73* (2011). URL
453 ecat.ga.gov.au/geonetwork.
- 454 [36] Fishwick, S., Heintz, M., Kennett, B. L. N., Reading, A. M. & Yoshizawa, K. Steps in lithospheric thickness
455 within eastern Australia, evidence from surface wave tomography. *Tectonics* **27** (2008).
- 456 [37] Hirschmann, M. M. Mantle solidus: Experimental constraints and the effects of peridotite composition.
457 *Geochemistry Geophysics Geosystems* **1** (2000).
- 458 [38] Grose, C. J. & Afonso, J. C. Comprehensive plate models for the thermal evolution of oceanic lithosphere.
459 *Geochemistry, Geophysics, Geosystems* **14** (2013).

- 460 [39] Taylor, W. R. An experimental test of some geothermometer and geobarometer formulations for upper mantle
461 peridotites with application to the thermobarometry of fertile lherzolite and garnet websterite. *Neues Jahrbuch*
462 *für Mineralogie - Abhandlungen* **172**, 381–408 (1998).
- 463 [40] Nickel, K. G. & Green, D. H. Empirical geothermobarometry for garnet peridotites and implications for the
464 nature of the lithosphere, kimberlites and diamonds. *Earth and Planetary Science Letters* **73**, 158–170 (1985).
- 465 [41] Nimis, P. & Grütter, H. Internally consistent geothermometers for garnet peridotites and pyroxenites. *Con-*
466 *tributions to Mineralogy and Petrology* **159**, 411–427 (2010).
- 467 [42] Nimis, P. & Taylor, W. R. Single clinopyroxene thermobarometry for garnet peridotites. Part I. Calibration
468 and testing of a Cr-in-Cpx barometer and an enstatite-in-Cpx thermometer. *Contributions to Mineralogy and*
469 *Petrology* **139**, 541–554 (2000).
- 470 [43] McKenzie, D. P., Jackson, J. & Priestley, K. Thermal structure of oceanic and continental lithosphere. *Earth*
471 *and Planetary Science Letters* **233**, 337–349 (2005).
- 472 [44] Mather, K. A., Pearson, D. G., McKenzie, D. P., Kjarsgaard, B. A. & Priestley, K. Constraints on the depth
473 and thermal history of cratonic lithosphere from peridotite xenoliths, xenocrysts and seismology. *Lithos* **125**,
474 729–742 (2011).
- 475 [45] Osako, M., Ito, E. & Yoneda, A. Simultaneous measurements of thermal conductivity and thermal diffusivity
476 for garnet and olivine under high pressure. *Physics of the Earth and Planetary Interiors* **143-144**, 311–320
477 (2004).
- 478 [46] Jaupart, C., Labrosse, S. & Mareschal, J. C. Temperatures, Heat and Energy in the Mantle of the Earth.
479 *Treatise on Geophysics* **7**, 253–303 (2007).
- 480 [47] Kennett, B. L. N., Salmon, M., Saygin, E. & Group, A. W. AusMoho: The variation of Moho depth in
481 Australia. *Geophysical Journal International* **187**, 946–958 (2011).
- 482 [48] Katz, R. F., Spiegelman, M. & Langmuir, C. H. A new parameterization of hydrous mantle melting. *Geo-*
483 *chemistry, Geophysics, Geosystems* **4** (2003).
- 484 [49] Shorttle, O., MacLennan, J. & Lambart, S. Quantifying lithological variability in the mantle. *Earth and*
485 *Planetary Science Letters* **395**, 24–40 (2014).
- 486 [50] Dalton, C. A., Ekström, G. & Dziewonski, A. M. Global seismological shear velocity and attenuation: A
487 comparison with experimental observations. *Earth and Planetary Science Letters* **284**, 65–75 (2009).
- 488 [51] Lau, H. C. *et al.* Inferences of mantle viscosity based on ice age data sets: Radial structure. *Journal of*
489 *Geophysical Research: Solid Earth* **121**, 6991–7012 (2016).
- 490 [52] Jain, C., Korenaga, J. & Karato, S. I. On the grain size sensitivity of olivine rheology. *Journal of Geophysical*
491 *Research: Solid Earth* **123**, 674–688 (2018).

- 492 [53] Kennett, B. L. N., Fichtner, A., Fishwick, S. & Yoshizawa, K. Australian seismological reference model
493 (AuSREM): Mantle component. *Geophysical Journal International* **192**, 871–887 (2013).
- 494 [54] Yoshizawa, K. & Kennett, B. L. N. Multimode surface wave tomography for the Australian region using a
495 three-stage approach incorporating finite frequency effects. *Journal of Geophysical Research: Solid Earth* **109**,
496 1–19 (2004).
- 497 [55] Fichtner, A., Kennett, B. L. N., Igel, H. & Bunge, H.-P. Full waveform tomography for radially anisotropic
498 structure: New insights into present and past states of the Australasian upper mantle. *Earth and Planetary
499 Science Letters* **290**, 270–280 (2010).
- 500 [56] Fichtner, A., Igel, H., Bunge, H.-P. & Kennett, B. L. N. Simulation and inversion of seismic wave propagation
501 on continental scales based on a spectral-element method. *Journal of Numerical Analysis, Industrial and
502 Applied Mathematics* **4**, 11–22 (2009).
- 503 [57] Fichtner, A., Kennett, B. L. N., Igel, H. & Bunge, H.-P. Full seismic waveform tomography for upper-mantle
504 structure in the Australasian region using adjoint methods. *Geophysical Journal International* **179**, 1703–1725
505 (2009).
- 506 [58] Yoshizawa, K. Radially anisotropic 3-D shear wave structure of the Australian lithosphere and asthenosphere
507 from multi-mode surface waves. *Physics of the Earth and Planetary Interiors* **235**, 33–48 (2014).
- 508 [59] Davies, D. R., Rawlinson, N., Iaffaldano, G. & Campbell, I. H. Lithospheric controls on magma composition
509 along Earth’s longest continental hotspot track. *Nature* **525**, 511–514 (2015).
- 510 [60] Czarnota, K., Roberts, G. G., White, N. J. & Fishwick, S. Spatial and temporal patterns of Australian dynamic
511 topography from river profile modeling. *Journal of Geophysical Research: Solid Earth* **119**, 1384–1424 (2014).
- 512 [61] Artemieva, I. M. Global 1 1 thermal model TC1 for the continental lithosphere: Implications for lithosphere
513 secular evolution. *Tectonophysics* **416**, 245–277 (2006).
- 514 [62] Bird, P., Liu, Z. & Rucker, W. K. Stresses that drive the plates from below: Definitions, computational path,
515 model optimization, and error analysis. *Journal of Geophysical Research: Solid Earth* **113** (2008).
- 516 [63] Steinberger, B. & Becker, T. W. A comparison of lithospheric thickness models. *Tectonophysics* 1–14 (2016).
- 517 [64] Pasyanos, M. E., Masters, T. G., Laske, G. & Ma, Z. LITHO1.0: An updated crust and lithospheric model of
518 the Earth. *Journal of Geophysical Research: Solid Earth* **119**, 2153–2173 (2014).

519 **Acknowledgments:** We are grateful to B. Steinberger, N. Rawlinson, K. Yoshizawa and B. Kennett for sharing
520 lithospheric thickness maps. We thank J.C. Afonso, J. Austermann, G. Begg, R. Blewett, A. Bufe, D. Champion,
521 R. Davies, B. Delbridge, M. Doublier, R. Fu, S. Goes, A. Gorbatov, B. Hodgin, B. Holtzman, J. Kingslake, T.
522 Mackey, D. McKenzie, J. Mitrovica, D. Müller, P. Nimis, E. Powell, K. Priestley, D. Schutt, O. Shorttle, R. Skirrow,
523 S. Stephenson, Y. Takei & J. Winterbourne for their assistance and discussions. This work is a contribution to

524 the Australian Government’s Exploring for the Future program. KC and DH publish with the permission of the
525 CEO of Geoscience Australia. MH acknowledges support from the National Aeronautics and Space Administration
526 grant NNX17AE17G and the American Chemical Society Petroleum Research Fund 59062-DNI8. FR acknowledges
527 support from the Schmidt Science Fellows program, in partnership with the Rhodes Trust.

528 **Author contributions:** This study was conceived by KC. KC and DH compiled deposit databases. LJ collated
529 Australian xenolith data. Thermobarometry was done by LJ, FR and MH. Paleogeotherm modelling was done
530 by FR and LJ. FR and MH developed shear-wave to temperature conversion scheme. FR calibrated anelasticity
531 parameterisations. MH generated LAB maps, performed statistical tests, made figures and compiled supplementary
532 materials. The paper was written by KC and MH, with guidance from all authors.

533 **Competing interests:** The authors declare no competing financial interests.

534 **Data availability:** All data is available in the manuscript or the supplementary materials. Correspondence should
535 be addressed to K. Czarnota (karol.czarnota@ga.gov.au) and M. Hoggard (mark_hoggard@fas.harvard.edu).

536 **Supplementary Information:**

- 537 • Additional Materials
- 538 • Figures S1–S20
- 539 • References (54–64)

540 **Supplementary Information for “Gigayear stability of**
541 **cratonic edges controls global distribution of**
542 **sediment-hosted metals”**

543 Karol Czarnota^{*,1,2}, Mark J. Hoggard^{*,3,4}, Fred D. Richards³, David L. Huston¹ & A. Lynton Jaques²

544 1. Geoscience Australia, GPO Box 378, Canberra ACT 2601, Australia.

545 2. Research School of Earth Sciences, Australian National University, Canberra, ACT 0200, Australia

546 3. Department of Earth & Planetary Sciences, Harvard University, 20 Oxford Street, Cambridge, MA 02138,
547 USA.

548 4. Lamont-Doherty Earth Observatory, Columbia University, 61 Rte 9W, Palisades, NY 10964, USA.

549 *karol.czarnota@ga.gov.au; mark_hoggard@fas.harvard.edu

550 **Contents**

- 551 1. Summary and comparison of regional seismic tomography models for Australia.
- 552 2. Compilation of fifteen Australian paleogeotherms obtained from xenolith thermobarometry.
- 553 3. Calibration and temperature conversion of seismic tomography models.
- 554 4. Regional lithospheric thickness maps for Australia calibrated in this study.
- 555 5. Previously published lithospheric thickness maps for Australia.
- 556 6. Histogram of global lithospheric thickness.
- 557 7. Maps of previously published global lithosphere-asthenosphere boundary depth.
- 558 8. Examples of random sets of continental locations for statistical tests.
- 559 9. Compilations and statistical tests for six major classes of base metal deposit.

560 **Additional Supporting Information (Files uploaded separately)**

- 561 1. Global and Australian lithospheric thickness maps in ASCII format.
- 562 2. Database of six major classes of base metal deposit.
- 563 3. Location and diopside compositions for xenocryst thermobarometry.
- 564 4. Fifteen Australian FITPLOT geotherms in ASCII format.

565 Seismic Tomography Model Comparison

566 Our LAB maps are based on the most recent, high-resolution shear wave tomography models. For the global map,
567 we use SL2013sv¹⁷ which is an upper mantle-only model built from a combination of body and surface waves,
568 including fundamental and higher modes. Periods considered are 11–450 s, $\sim 750,000$ seismograms are included,
569 and misfits are calculated between synthetics and the full waveform up to the 9th overtone. Crucially, simultaneous
570 inversion for the crustal model results in minimal smearing of slow crustal velocities down into the upper mantle,
571 thereby allowing us to use more depth slices in our V_S to temperature calibration. Checkerboard resolution tests
572 indicate that features ~ 600 km in diameter at lithospheric depths are generally well resolved. Finer features should
573 be resolvable in regions with dense ray path coverage, such as North America, Europe and southeast Asia.

574 The SL2013sv model contains only 6 seismometers in Australia, so has limited resolution within this continent.
575 Therefore, we also investigate three regional seismic tomography models to generate high resolution maps for the
576 Australian continent. The main model used throughout this paper is the radially isotropic V_S model FR12¹⁶, which
577 is derived from Rayleigh wave travel times.³⁶ Periods considered are 50–120 s and the fundamental and first four
578 higher modes have been used where possible, leading to good sensitivity down to ~ 250 km depths. It contains
579 a greater number of source–receiver paths ($> 13,000$) compared to other Australian models. However, it uses
580 an *a priori* crustal model that remains fixed throughout the inversion, resulting in noticeable smearing of crustal
581 velocities into the upper mantle. Checkerboard tests indicate that features ~ 300 km in diameter at lithospheric
582 depths are well resolved.

583 The second regional model is AuSREM⁵³ and is a hybrid model constructed by linear combination of several
584 previous studies. It combines FR12 with YK04⁵⁴ and AMSAN.19.⁵⁵ YK04 is a radially anisotropic Rayleigh wave
585 model using > 8000 ray paths for the fundamental mode and ~ 2000 for the first three higher modes, yielding a
586 maximum period range of 40–150 s. It includes off-great circle and finite frequency effects, but also uses a fixed
587 crustal model. AMSAN.19 is a radially anisotropic, 3D waveform, spectral element model that uses an inversion
588 scheme based on the adjoint approach.^{56,57} Periods considered are 30–200 s and a fixed crustal model is used. Due
589 to the computationally intensive methodology, $\sim 3,000$ waveforms are used in this inversion.

590 The third and final regional model considered in this study is the radially anisotropic Y14.⁵⁸ It combines
591 Rayleigh waves (8000 fundamental, ~ 2500 higher mode) and Love waves (approximately two-thirds as many) with
592 periods ~ 25 –200s, corrected for local crustal structure using a fixed crustal model. It adopts the same three-step
593 inversion procedure as YK04.⁵⁴ All three models are plotted alongside the global SL2013sv model in Figures S1, S2
594 and S3. At any given location within the continent, V_S varies between models by ~ 0.1 km s⁻¹.

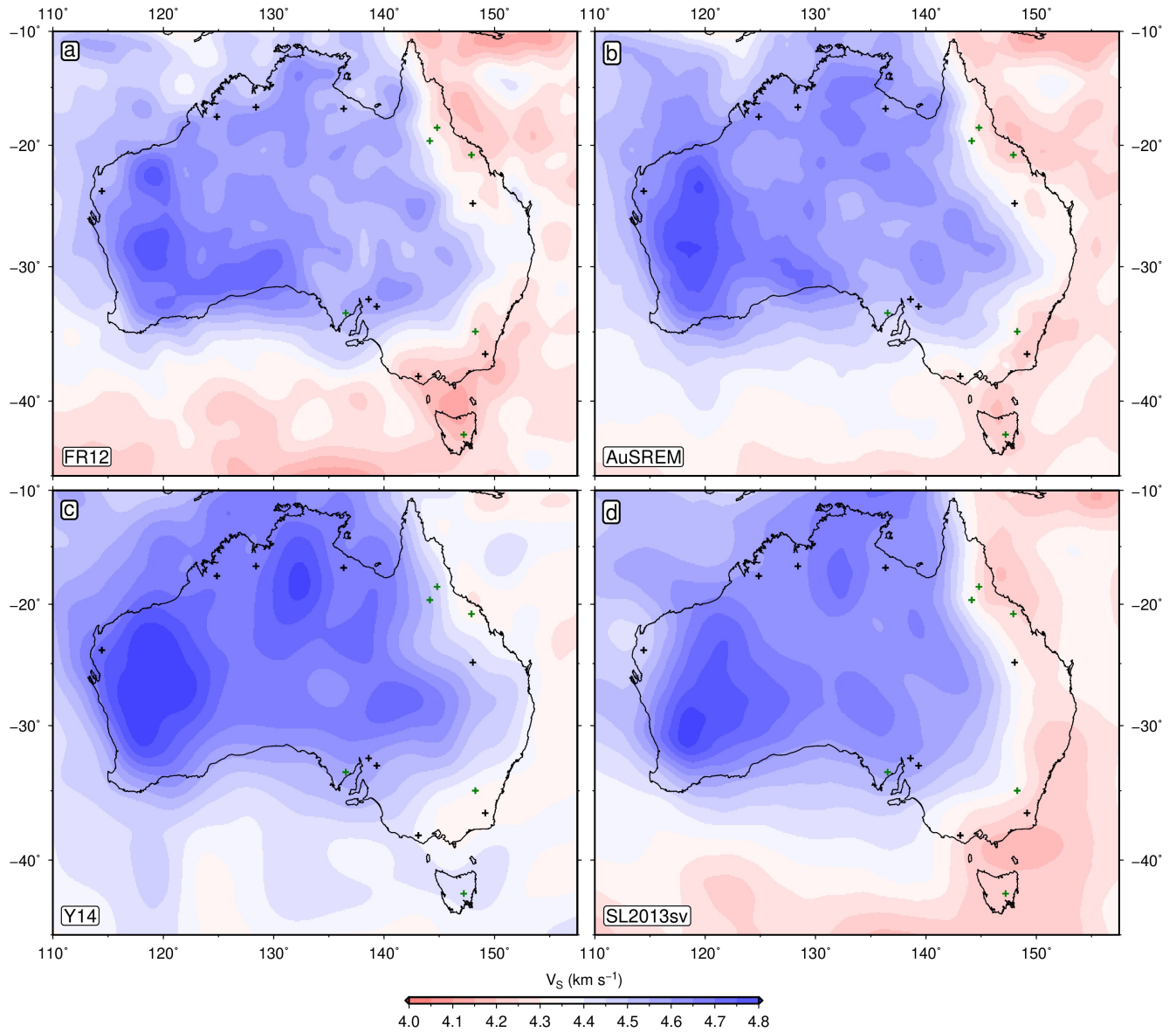


Figure S1: 100 km depth slice through Australian seismic tomography models. Black/green crosses = paleogeotherms used as constraints/tests in anelasticity calibration. (a) FR12 = regional isotropic V_S ¹⁶. (b) AuSREM = regional V_{SV} ⁵³. (c) Y14 = regional V_{SV} ⁵⁸. (d) SL2013sv = global V_{SV} ¹⁷.

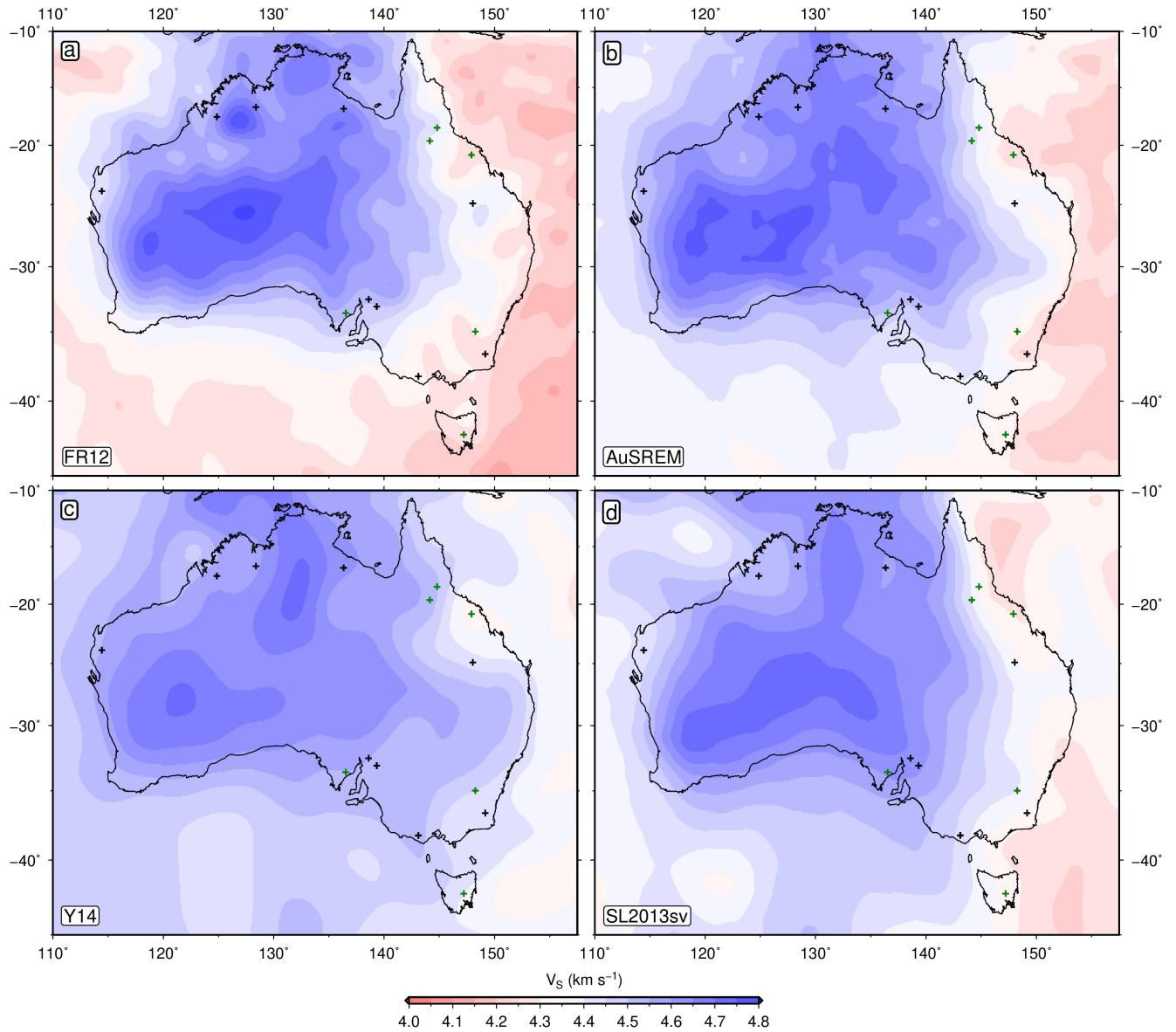


Figure S2: 175 km depth slice through Australian seismic tomography models. Black/green crosses = paleogeotherms used as constraints/tests in anelasticity calibration. (a) FR12 = regional isotropic V_S ¹⁶. (b) AuSREM = regional V_{SV} ⁵³. (c) Y14 = regional V_{SV} ⁵⁸. (d) SL2013sv = global V_{SV} ¹⁷.

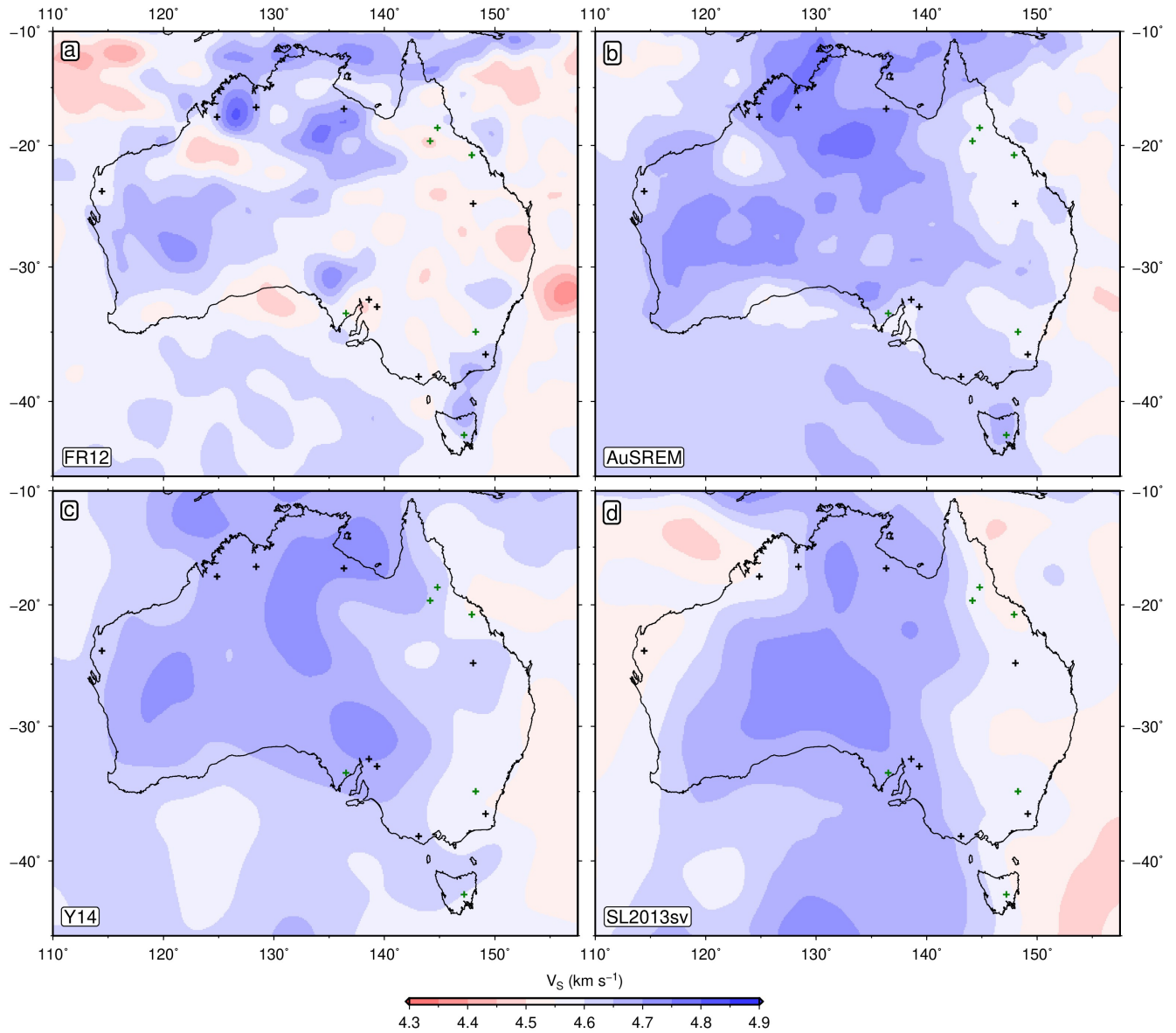


Figure S3: 250 km depth slice through Australian seismic tomography models. Black/green crosses = paleogeotherms used as constraints/tests in anelasticity calibration. (a) FR12 = regional isotropic V_S ¹⁶. (b) AuSREM = regional V_{SV} ⁵³. (c) Y14 = regional V_{SV} ⁵⁸. (d) SL2013sv = global V_{SV} ¹⁷.

595 Thermobarometry and Regional Calibration of Tomography Models

596 Temperature estimates across a range of depths are required to generate a series of V_S -T-P tie points in order
597 to calibrate the regional seismic tomography models. We therefore assemble a suite of Australian paleogeotherms
598 derived from thermobarometric analysis of mantle xenoliths and xenocrysts from fifteen locations in thick and thin
599 lithosphere (Figure S4). The resulting P-T estimates are entered into FITPLOT to generate the palaeogeotherms
600 shown in Figure S5 (Methods).

601 The results of regional calibration using the paleogeotherms are shown in Figures S6 and S7. Note that the
602 global model SL2013sv yields good fits to paleogeotherms away from south Australia (Monk Hill, Orroroo and
603 Cleve), despite being lower resolution than the local models and being calibrated completely independently of this
604 information (red lines in Figure S7). Conversely, regional models often provide a poorer fit to the full range of
605 the paleogeotherms and can exhibit substantial crustal bleeding artefacts at depths shallower than ~ 125 km.
606 Generally amongst the regional models, FR12 performs the best, followed by AuSREM and then Y14.

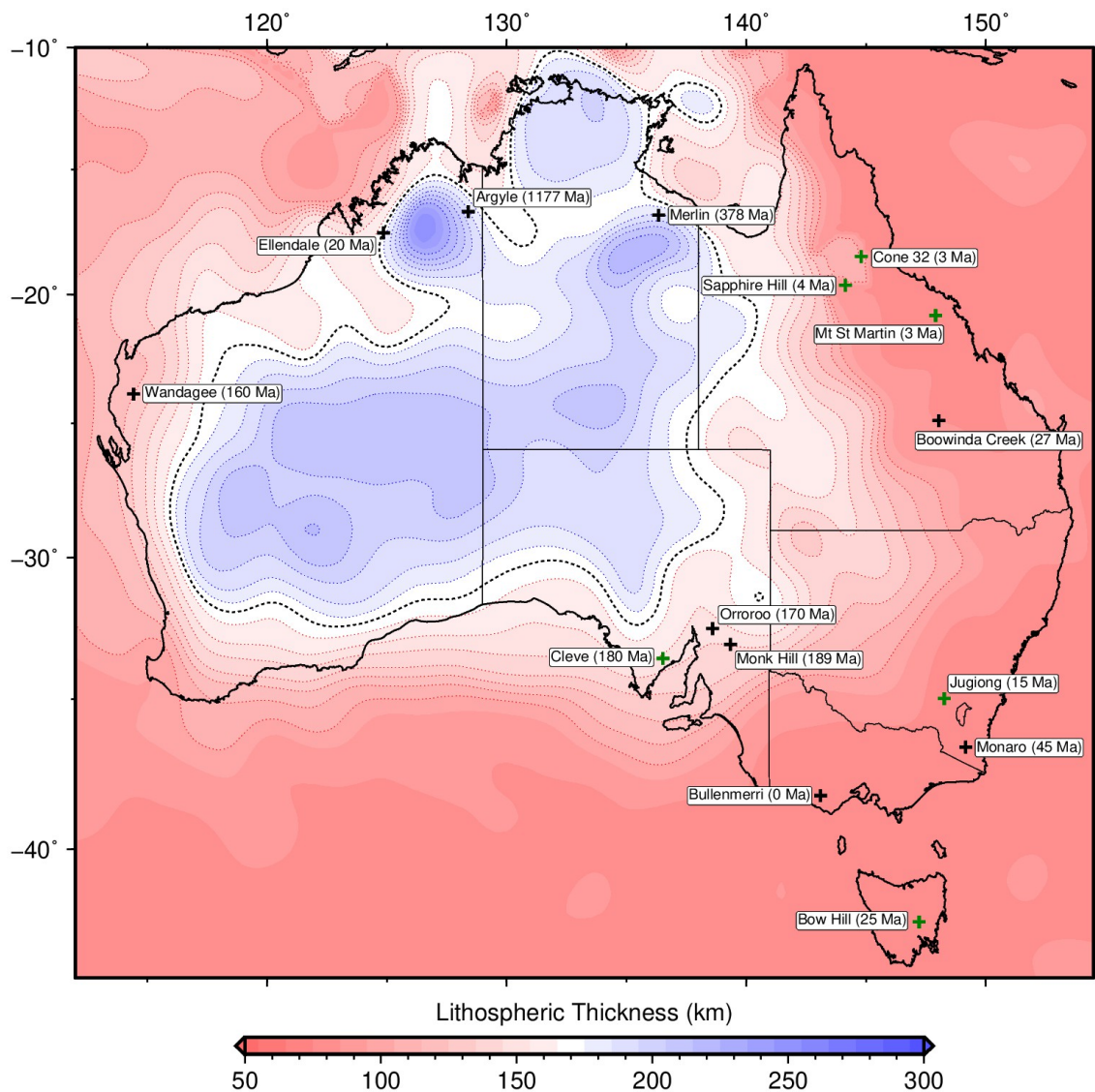


Figure S4: **Location of Australian xenolith and xenocryst suites.** Labels give site name and age (in million years); black crosses = locations used to constrain anelasticity calibration, green crosses = locations used to visually test validity of results; red/blue colours = lithospheric thickness (from Figure 1b), derived from FR12 seismic tomography model.¹⁶

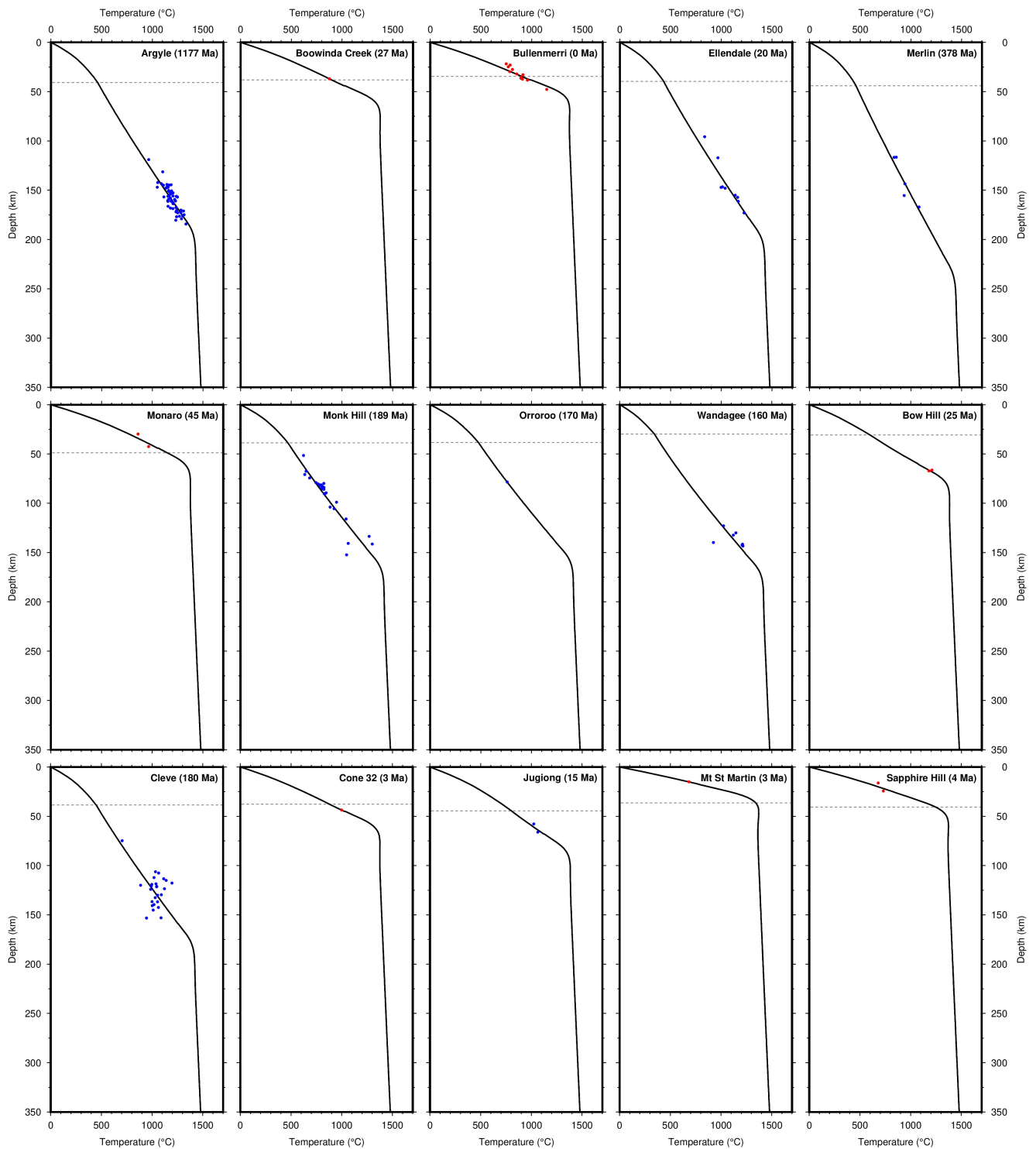


Figure S5: **Australian paleogeotherms derived from xenolith and xenocryst thermobarometry.** Labels give site name and age (in million years) from Figure S4; red circles = P-T estimates derived from multiphase thermobarometry^{40,39}; blue circles = P-T estimates derived from single chrome diopside thermobarometry⁴²; dashed line = crustal thickness from AusMoho⁴⁷; solid line = FITPLOT optimal paleogeotherm.

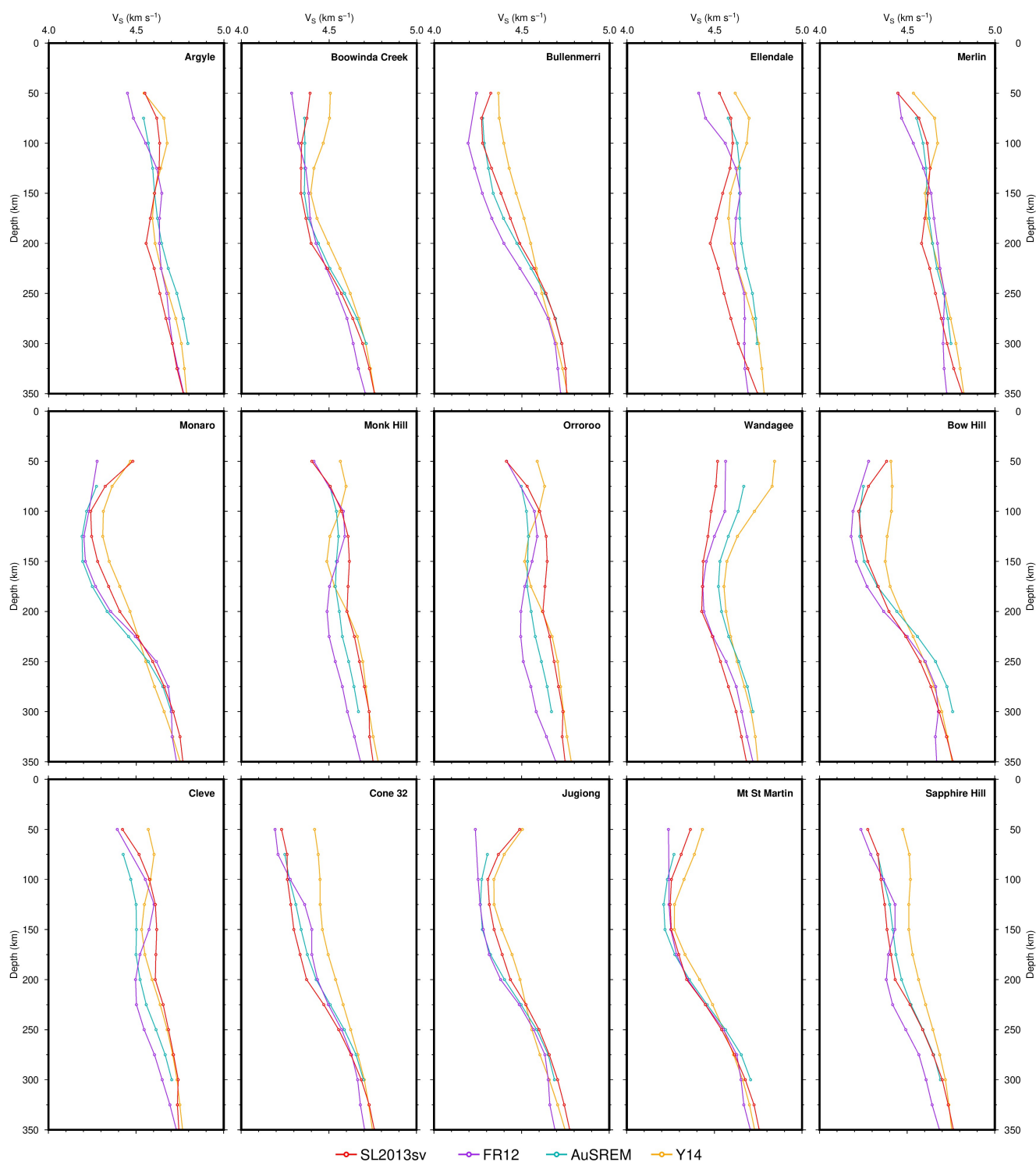


Figure S6: V_S as a function of depth at sites of fifteen Australian paleogeotherms. Labels give site name (locations in Figure S4); red = global SL2013sv model¹⁷; purple = regional FR12 model¹⁶; blue = regional AuSREM model⁵³; orange = regional Y14 model⁵⁸.

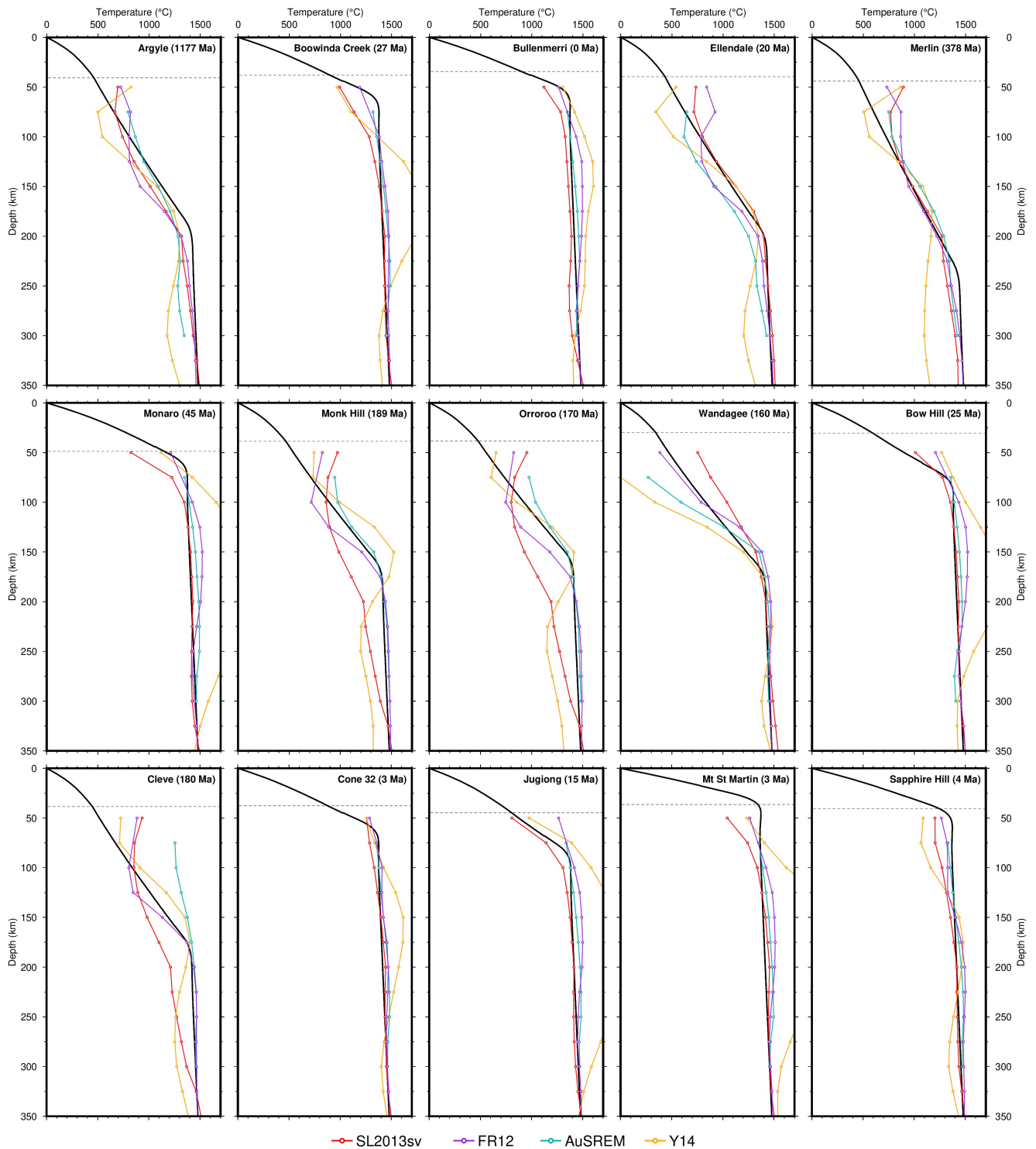


Figure S7: **Calibration of anelasticity parameterisation on Australian paleogeotherms.** Labels give site name and inferred age of paleogeotherms in million years (locations in Figure S4); sites Argyle to Wandagee are used to constrain calibration; sites Bow Hill to Sapphire Hill are used to visually check output; dashed line = crustal thickness from AusMoho⁴⁷; solid line = optimal FITPLOT geotherm from Figure S5; purple = regional FR12 model¹⁶; blue = regional AuSREM model⁵³; orange = regional Y14 model⁵⁸; red = global SL2013sv model¹⁷, for comparison, calibrated independently of palaeogeotherm constraints.

607 **Australian Lithospheric Thickness Maps**

608 For each of the individually calibrated seismic tomography models in this study, we have mapped out the LAB in
 609 a consistent manner. The resulting maps for Australia are shown in Figure S8, whilst in Figure S9 we compare our
 610 preferred FR12 regional model to previously published maps of LAB depth beneath Australia.

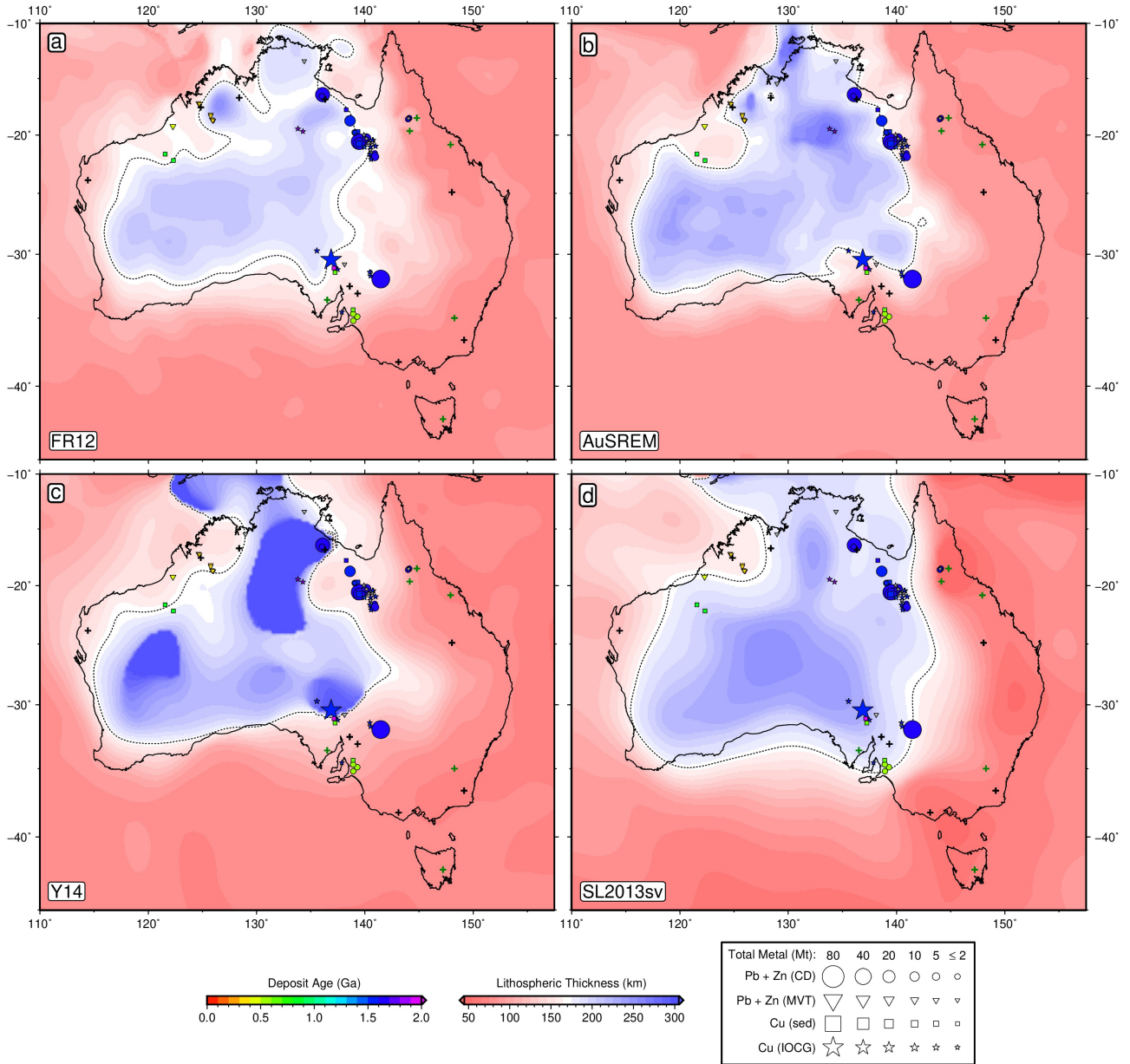


Figure S8: **Depth to lithosphere-asthenosphere boundary from individually calibrated Australian seismic tomography models.** Black contour = 170 km LAB thickness; green/black crosses = paleogeotherms used/unused in anelasticity calibration; other symbols = sediment-hosted deposit locations; area proportional to estimate of total contained mass of metal (MT = megatonnes); unknown deposit size given 2 Mt symbol; colour = ore body formation age (billion years); unknown age plotted in grey; circles = clastic-dominated lead-zinc (PbZn-CD); triangles = Mississippi Valley type lead-zinc (PbZn-MVT); squares = sedimentary copper (Cu-sed); stars = iron-oxide-copper-gold (IOCG). (a) based on FR12.¹⁶ (b) based on AuSREM.⁵³ (c) based on Y14.⁵⁸ (d) based on global SL2013sv.¹⁷

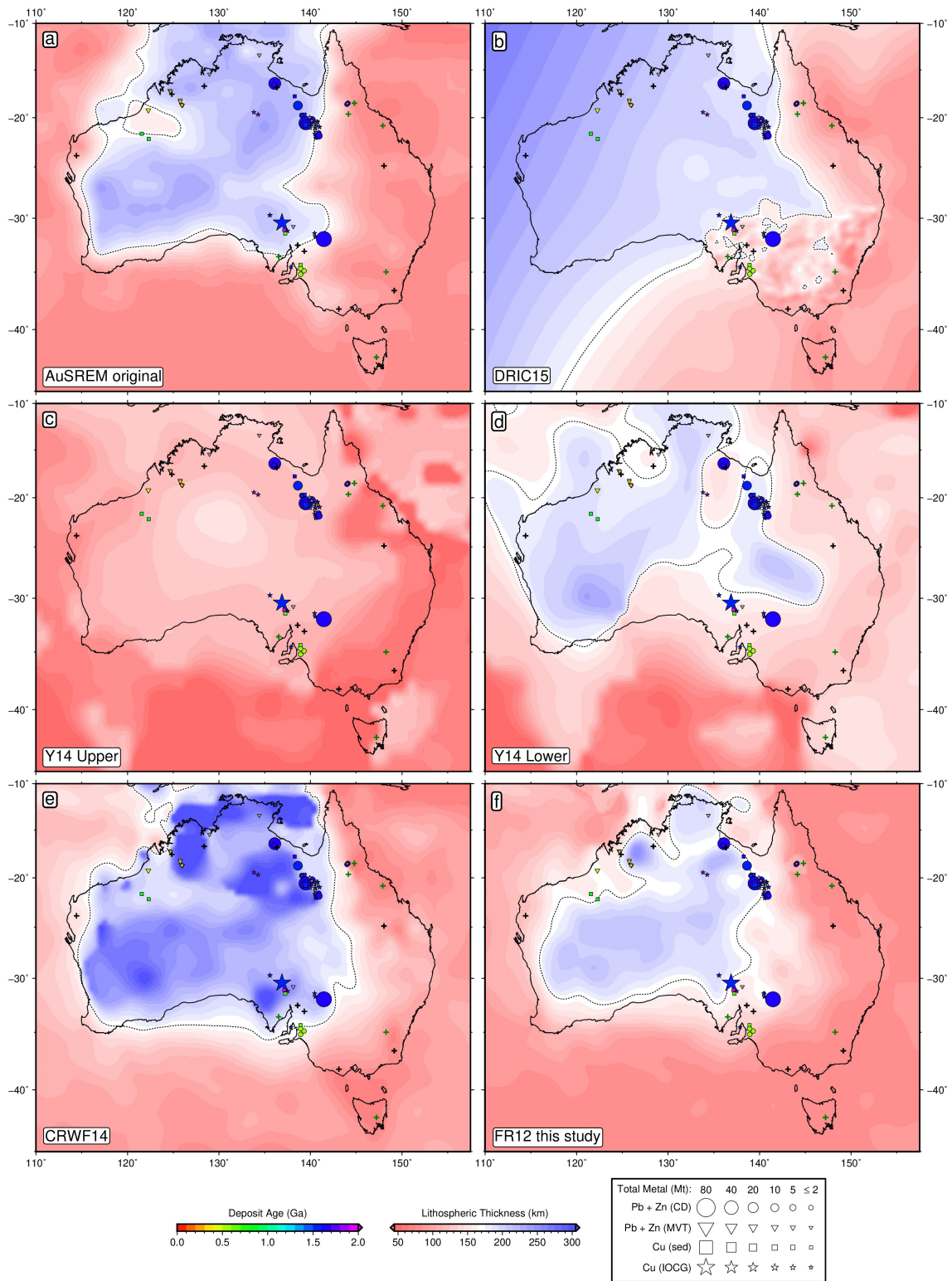


Figure S9: **Depth to lithosphere-asthenosphere boundary beneath Australia from previous studies.** Black contour = 170 km LAB thickness; green/white crosses = paleogeotherms used/unused in anelasticity calibration; other symbols = sediment-hosted deposit locations; area proportional to estimate of total contained mass of metal (MT = megatonnes); unknown deposit size given 2 Mt symbol; colour = ore body formation age (billion years); unknown age plotted in grey; circles = clastic-dominated lead-zinc (PbZn-CD); triangles = Mississippi Valley type lead-zinc (PbZn-MVT); squares = sedimentary copper (Cu-sed); stars = iron-oxide-copper-gold (IOCG). (a) Original AuSREM.⁵³ (b) DRIC15.⁵⁹ (c) Upper bound of Y14.⁵⁸ (d) Lower bound of Y14.⁵⁸ (e) CRWF14⁶⁰, derived using FR12 tomography.¹⁶ (f) FR12 LAB model generated in this study.

611 **Histogram of Global Lithospheric Thickness**

612 Global LAB thickness derived from the SL2013sv model¹⁷ reveals a bi-modal population with peaks at 80 km and
613 180 km, separated by a minimum at 150 km (Figure S10). There is also a noticeable drop-off deeper than 200 km,
614 which we attribute to a change in the gradient of V_S with depth in the initial starting profile used to construct the
615 tomography model.

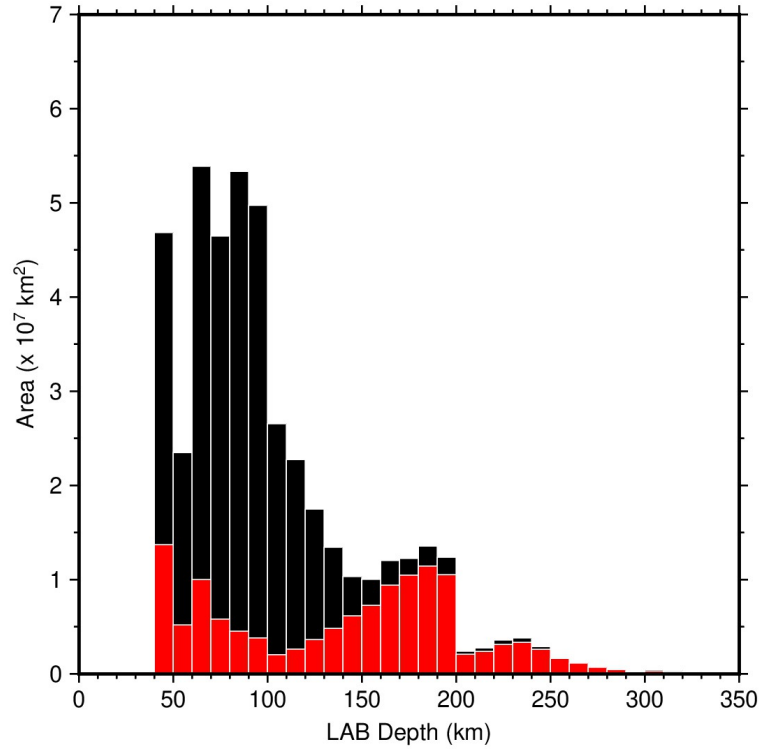


Figure S10: **Area-weighted histogram of global LAB depths.** LAB derived from the SL2013sv tomography model¹⁷; black bars = oceanic regions; red bars = continental regions.

616 **Previously Published Global LAB Maps**

617 For comparison, we provide five previously published global lithosphere-asthenosphere boundary (LAB) maps
 618 derived from a mixture of heat flow data and seismic tomography datasets. Interestingly, many giant sediment
 619 hosted mineral deposits lie along LAB edges defined by these other studies, testifying to the veracity of the observed
 620 relationship.

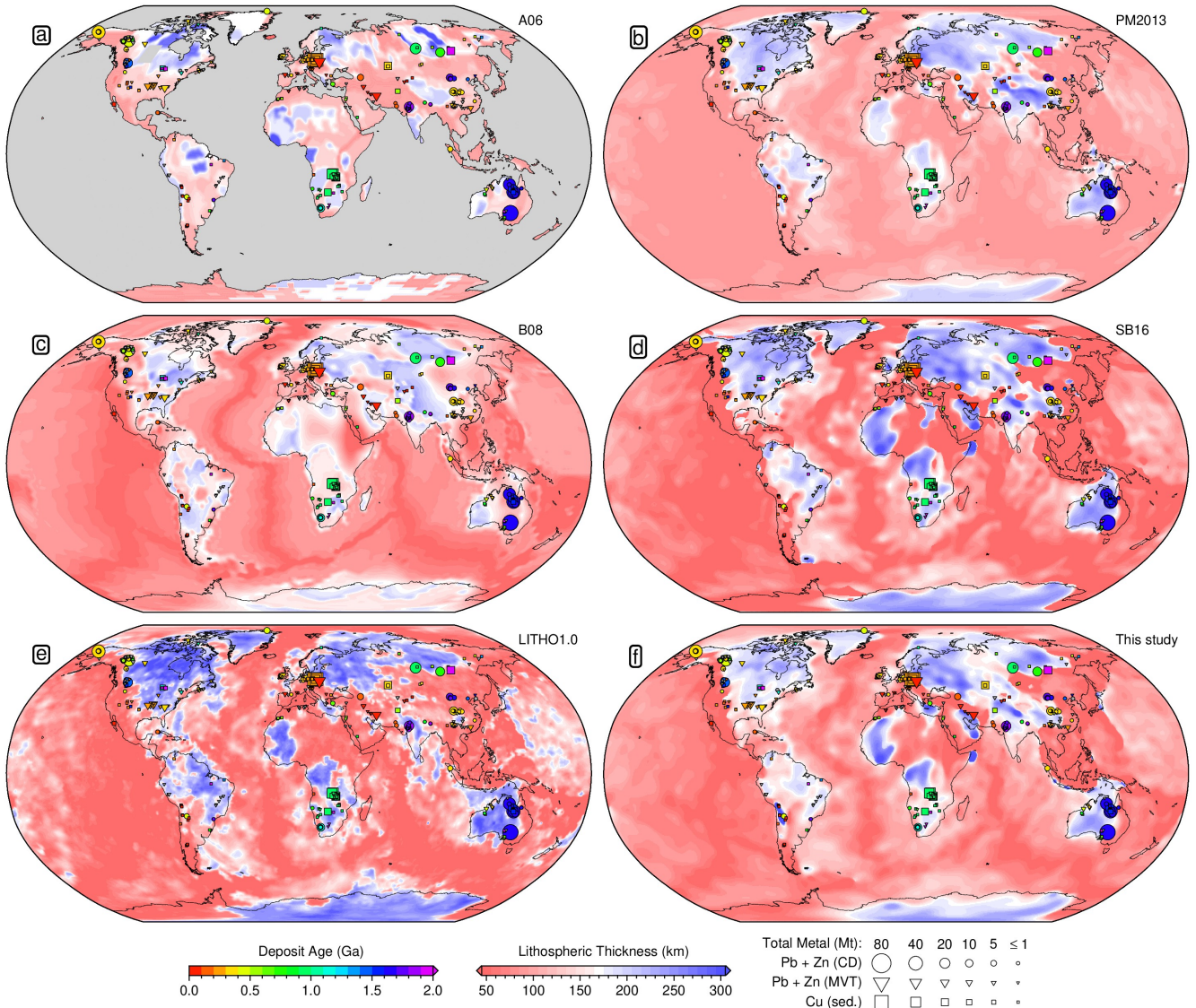


Figure S11: **Previously published global maps of depth to the lithosphere-asthenosphere boundary.** Symbols = sediment-hosted deposit locations; area proportional to estimate of total contained mass of metal (MT = megatonnes); unknown deposit size given 1 Mt symbol; colour = ore body formation age (billion years); unknown age plotted in grey; circles = clastic-dominated lead-zinc (PbZn-CD); triangles = Mississippi Valley type lead-zinc (PbZn-MVT); squares = sedimentary copper (Cu-sed). (a) LAB derived from surface heat flow measurements⁶¹; (b) LAB derived from surface wave tomography¹⁴; (c) LAB derived from vertical shear-wave travel time anomalies in the continents⁶²; (d) LAB⁶³ derived from SL2013sv tomography model¹⁷; (e) LAB derived from surface wave tomography⁶⁴; (f) LAB derived in this study using SL2013sv tomography model¹⁷.

621 Kolmogorov-Smirnov Statistical Tests

622 In order to test the statistical significance of real deposit locations, test suites of random points on a sphere are
623 generated. Example test suites of 100, 1000 and 10,000 points are shown in Figure S12.

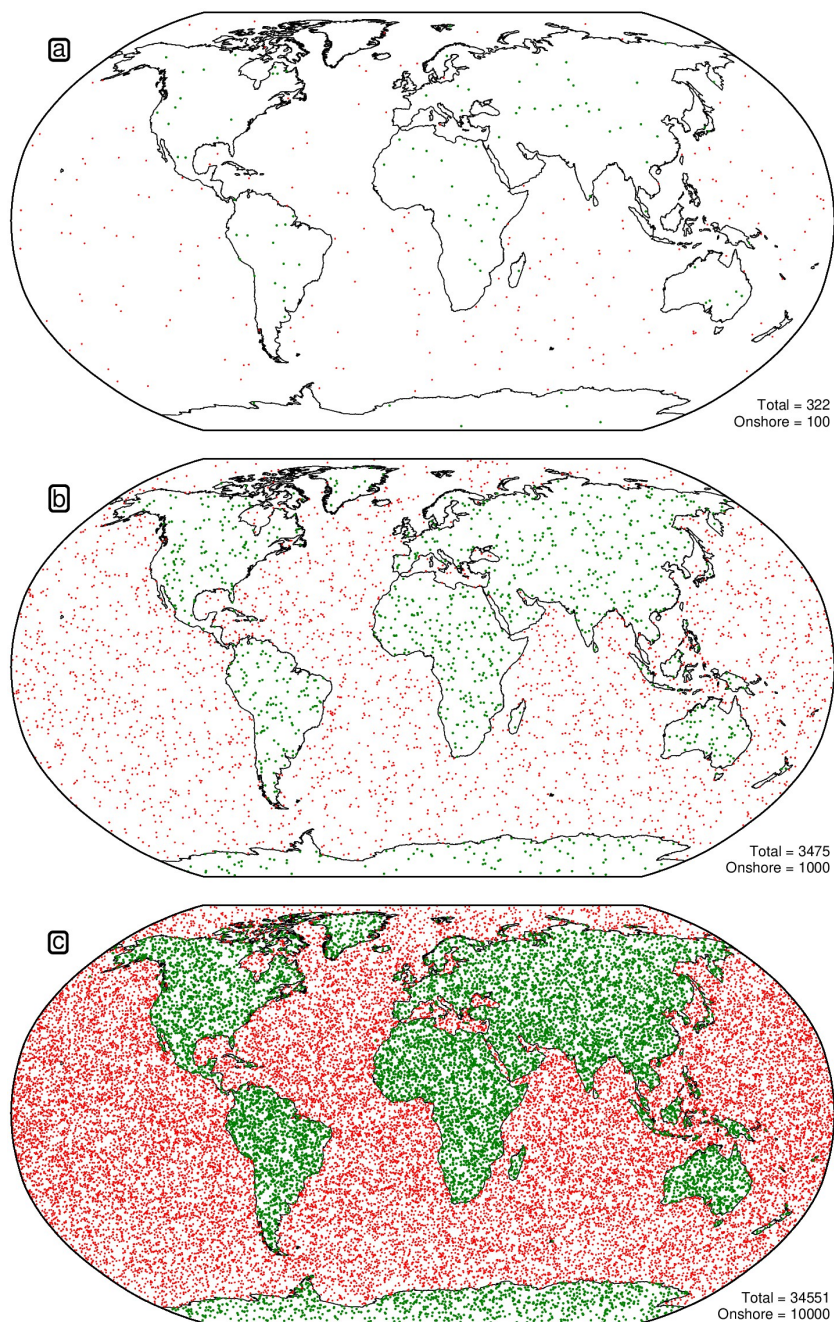


Figure S12: **Distribution of random points on the surface of a sphere.** Green circles = onshore points; red = offshore. (a) Example set of 100 onshore points. (b) Example set of 1000 onshore points. (c) Example set of 10,000 onshore points.

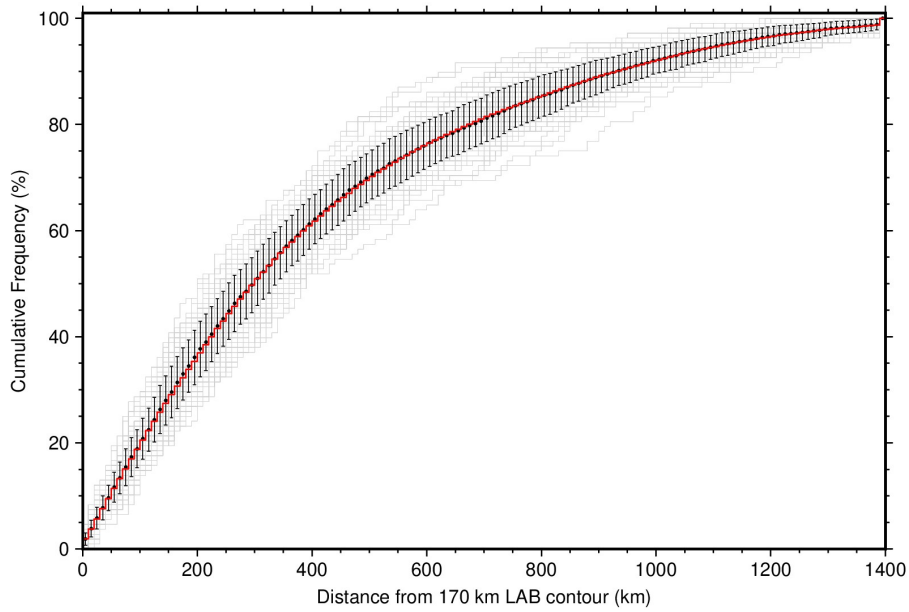


Figure S13: **Cumulative distribution functions for random continental points with distance from the 170 km LAB thickness contour.** Grey lines = 100 CDFs for a set of 109 random points in the continents; black points with error bars = mean and standard deviation of all 100 CDFs within each 10 km bin; red line = CDF for a set of 10,000 random continental points.

624 For each Kolmogorov-Smirnov test, a number of random points are generated that is equivalent to the number
 625 of real deposits of that type (109 for PbZn-CD, 147 for PbZn-MVT and 139 for sedimentary copper). Given the
 626 low sample size for some of the deposit classes, the distribution of this random set can vary somewhat from the true
 627 average distribution of continental locations. We therefore draw a test set in this manner 100 times (Figure S13).
 628 These random CDFs are relatively consistent but have some outliers. The D-value and Kolmogorov-Smirnov
 629 statistics between each random CDF and the real one is calculated and reported within a histogram (Figure S14).

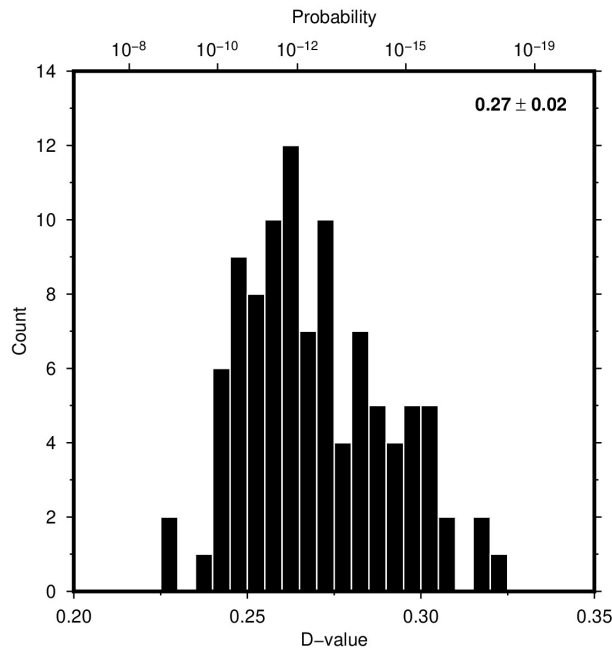


Figure S14: **D-values for all 395 sediment-hosted base metal deposits.** Histogram of D-values for ensemble of 100 random CDFs calculated for each random test set compared with the non-mass-weighted, locally enhanced CDF; inset lists mean and standard deviation of D-values; associated probabilities shown across top.

630 **Deposit Compilation**

631 Figures S15–S20 show deposit locations, age distributions with respect to LAB thickness, and Kolmogorov-Smirnov
 632 statistical test results for each individual deposit type.

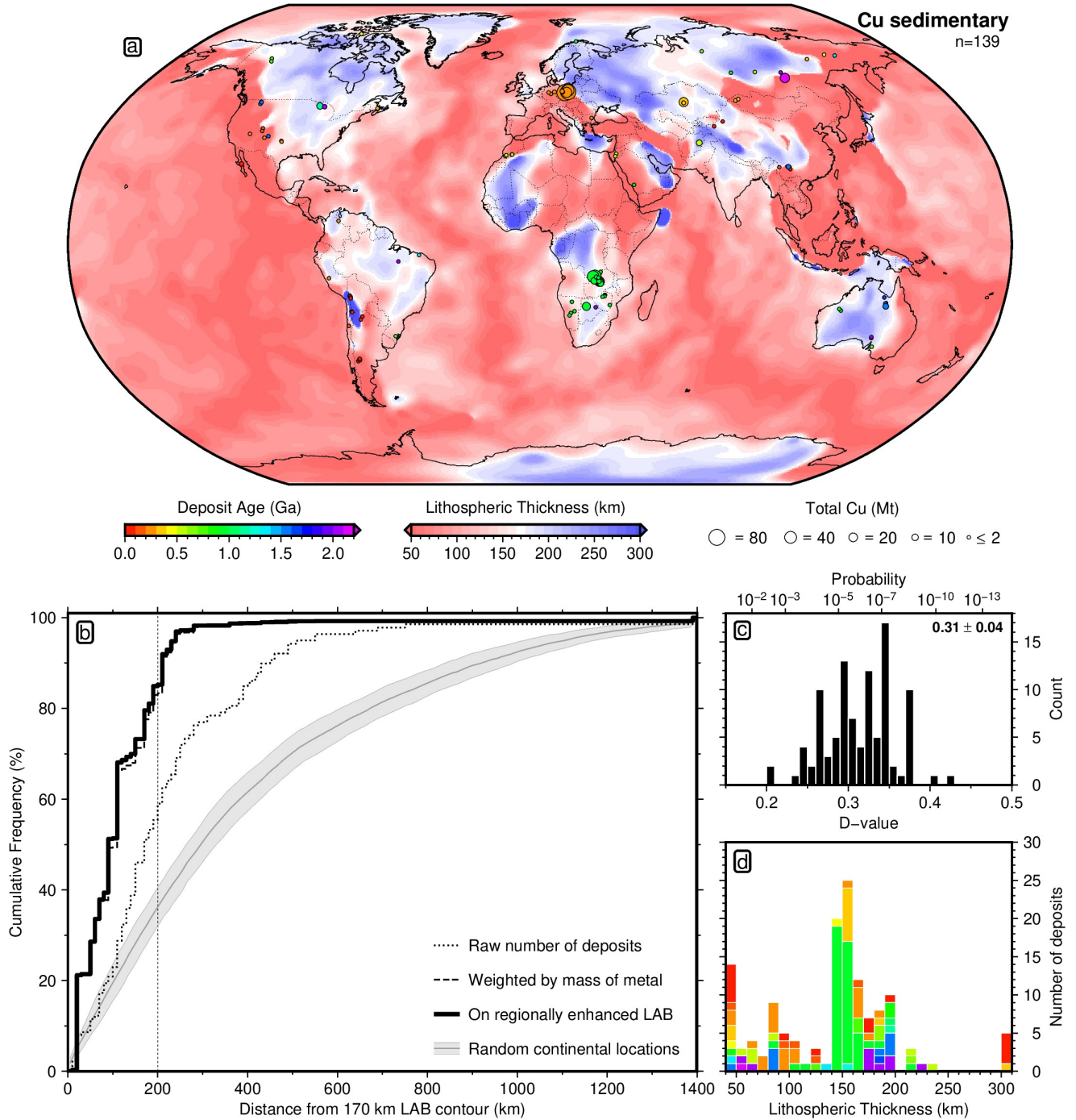


Figure S15: **139 sedimentary copper deposits**. (a) LAB derived from SL2013sv tomography model using a calibrated anelasticity parameterisation.^{17,15} Circles = deposit locations; area proportional to estimate of total contained mass of metal (MT = megatonnes); unknown deposit size given 2 Mt symbol; colour = ore body formation age (billion years); unknown age plotted in grey. (b) Different approaches for generating cumulative distribution functions. Dotted line = simple count of number of deposits with increasing distance from the 170 km contour in global LAB map; dashed line = weighting by contained mass of copper; solid black line = mass of metal-weighted deposits where Australian LAB has been replaced with regionally enhanced map (Figure S8a); grey line/bounds = mean and standard deviation of 100 sets of equivalent number of randomly drawn continental locations, with respect to regionally enhanced LAB. (c) Histogram of 100 D-values calculated for each random test set and a non-mass-weighted, locally enhanced CDF; inset lists mean and standard deviation of D-values; associated probabilities shown across top. (d) Histogram of deposit occurrence as a function of lithospheric thickness, coloured by deposit age.

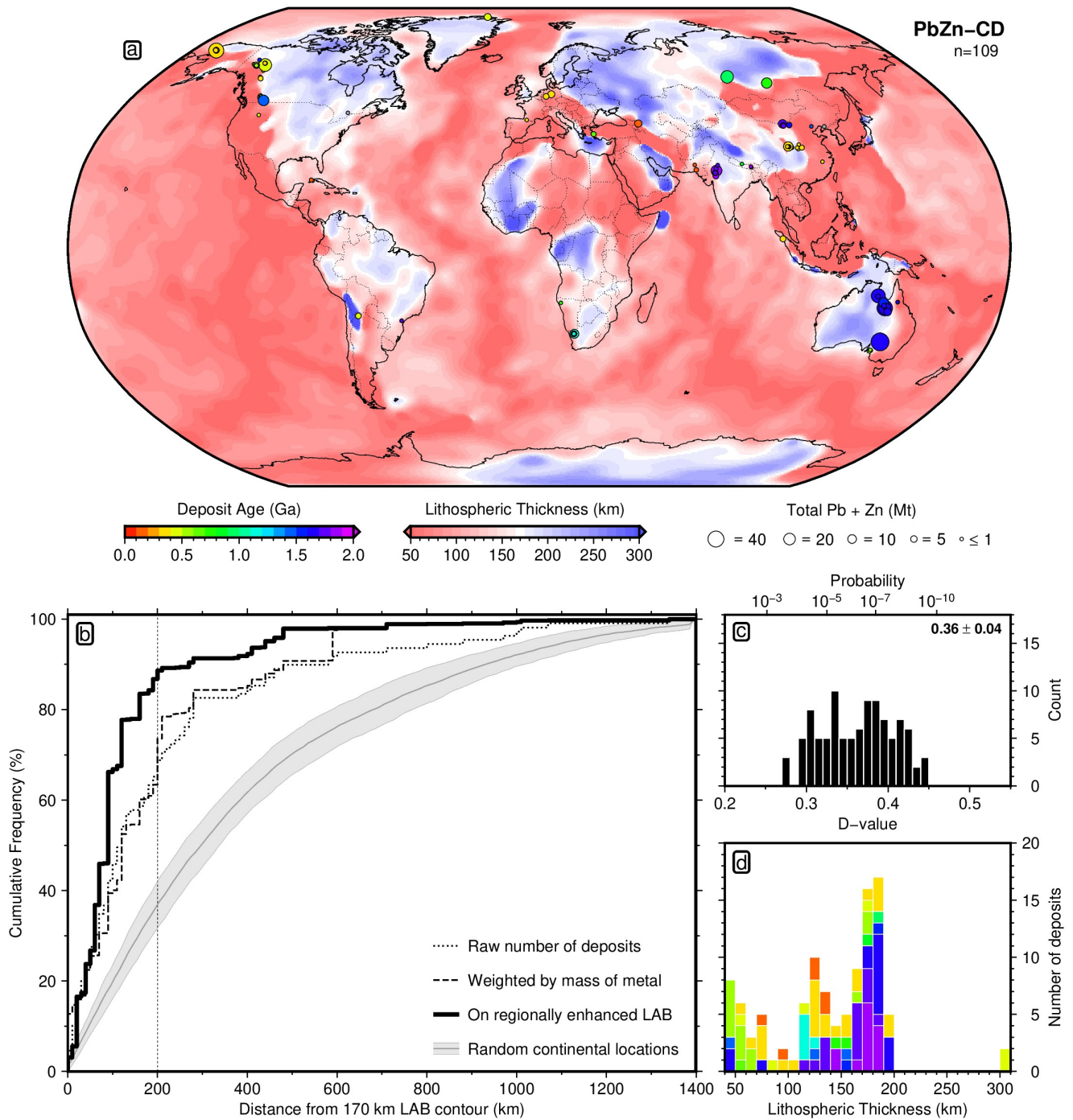


Figure S16: **109 clastic-dominated lead-zinc deposits.** (a) LAB derived from SL2013sv tomography model using a calibrated anelasticity parameterisation.^{17,15} Circles = deposit locations; area proportional to estimate of total contained mass of metal (MT = megatonnes); unknown deposit size given 1 Mt symbol; colour = ore body formation age (billion years); unknown age plotted in grey. (b) Different approaches for generating cumulative distribution functions. Dotted line = simple count of number of deposits with increasing distance from the 170 km contour in global LAB map; dashed line = weighting by contained mass of lead and zinc; solid black line = mass of metal-weighted deposits where Australian LAB has been replaced with regionally enhanced map (Figure S8a); grey line/bounds = mean and standard deviation of 100 sets of equivalent number of randomly drawn continental locations, with respect to regionally enhanced LAB. (c) Histogram of 100 D-values calculated for each random test set and a non-mass-weighted, locally enhanced CDF; inset lists mean and standard deviation of D-values; associated probabilities shown across top. (d) Histogram of deposit occurrence as a function of lithospheric thickness, coloured by deposit age.

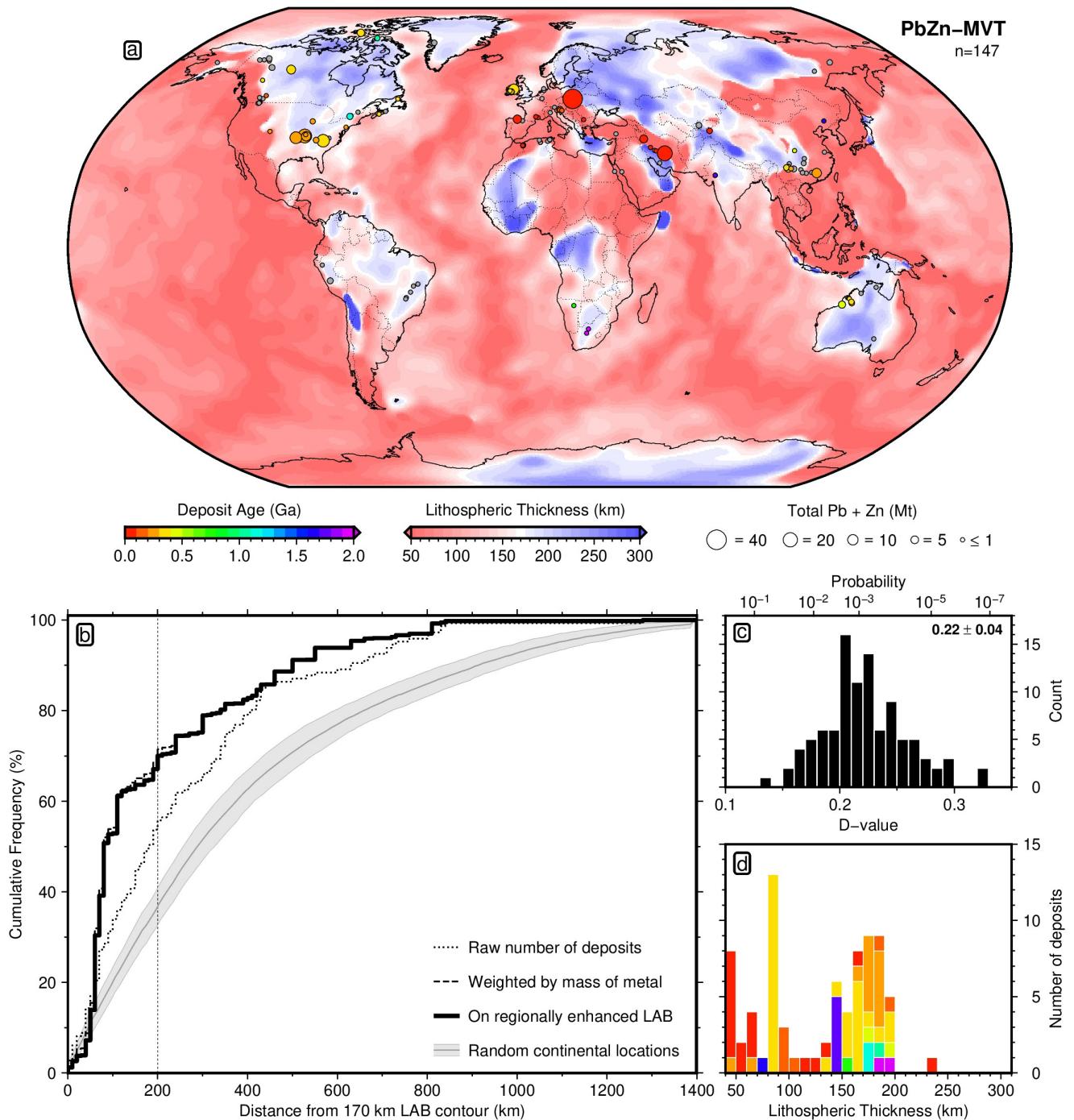


Figure S17: **147 Mississippi Valley-type lead-zinc deposits.** (a) LAB derived from SL2013sv tomography model using a calibrated anelasticity parameterisation.^{17,15} Circles = deposit locations; area proportional to estimate of total contained mass of metal (MT = megatonnes); unknown deposit size given 1 Mt symbol; colour = ore body formation age (billion years); unknown age plotted in grey. (b) Different approaches for generating cumulative distribution functions. Dotted line = simple count of number of deposits with increasing distance from the 170 km contour in global LAB map; dashed line = weighting by contained mass of lead and zinc; solid black line = mass of metal-weighted deposits where Australian LAB has been replaced with regionally enhanced map (Figure S8a); grey line/bounds = mean and standard deviation of 100 sets of equivalent number of randomly drawn continental locations, with respect to regionally enhanced LAB. (c) Histogram of 100 D-values calculated for each random test set and a non-mass-weighted, locally enhanced CDF; inset lists mean and standard deviation of D-values; associated probabilities shown across top. (d) Histogram of deposit occurrence as a function of lithospheric thickness, coloured by deposit age.

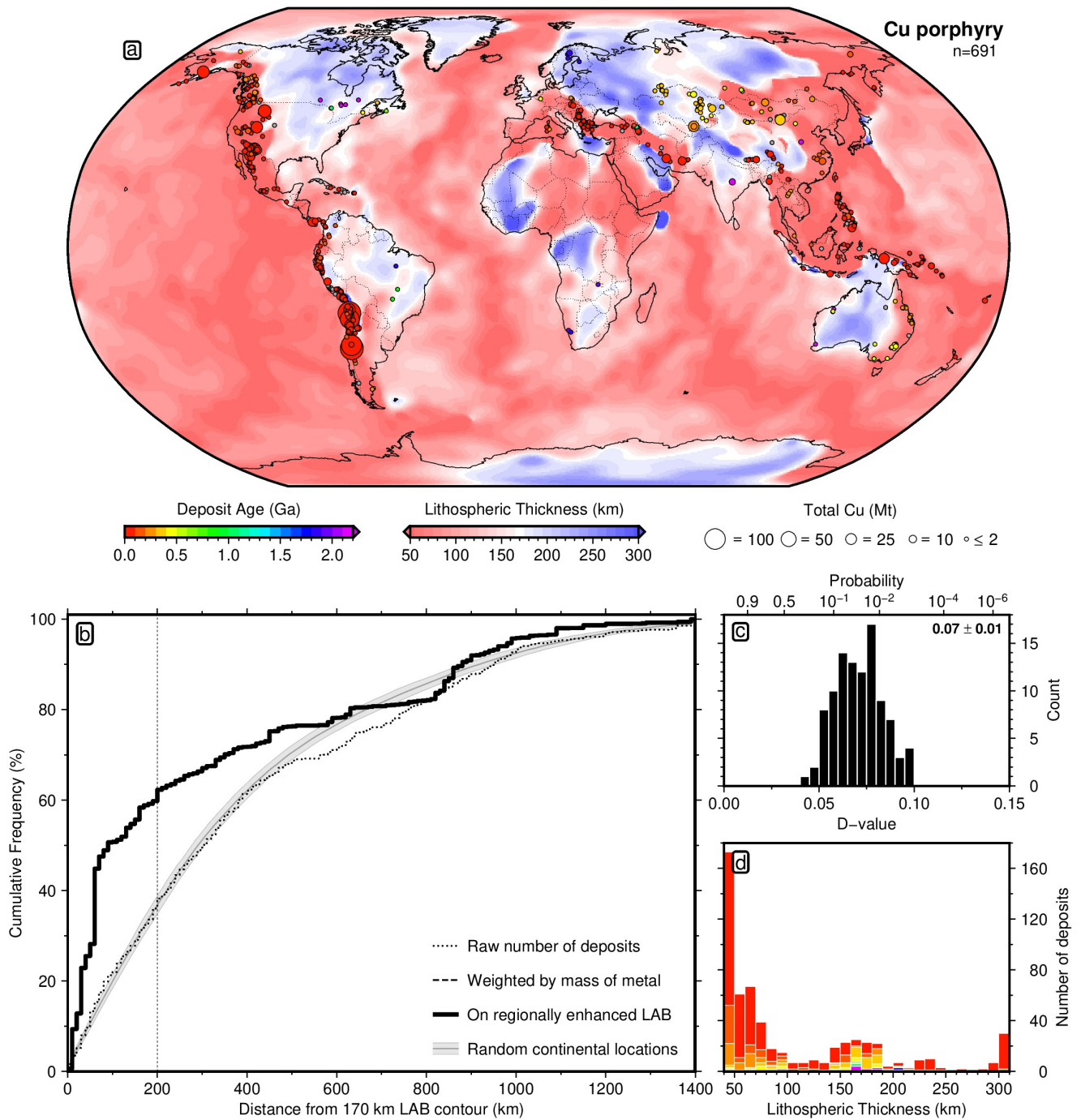


Figure S18: **691 copper porphyry deposits.** (a) LAB derived from SL2013sv tomography model using a calibrated anelasticity parameterisation.^{17,15} Circles = deposit locations; area proportional to estimate of total contained mass of metal (MT = megatonnes); unknown deposit size given 2 Mt symbol; colour = ore body formation age (billion years); unknown age plotted in grey. (b) Different approaches for generating cumulative distribution functions. Dotted line = simple count of number of deposits with increasing distance from the 170 km contour in global LAB map; dashed line = weighting by contained mass of copper; solid black line = mass of metal-weighted deposits where Australian LAB has been replaced with regionally enhanced map (Figure S8a); grey line/bounds = mean and standard deviation of 100 sets of equivalent number of randomly drawn continental locations, with respect to regionally enhanced LAB. (c) Histogram of 100 D-values calculated for each random test set and the a non-mass-weighted, locally enhanced CDF; inset lists mean and standard deviation of D-values; associated probabilities shown across top. (d) Histogram of deposit occurrence as a function of lithospheric thickness, coloured by deposit age.

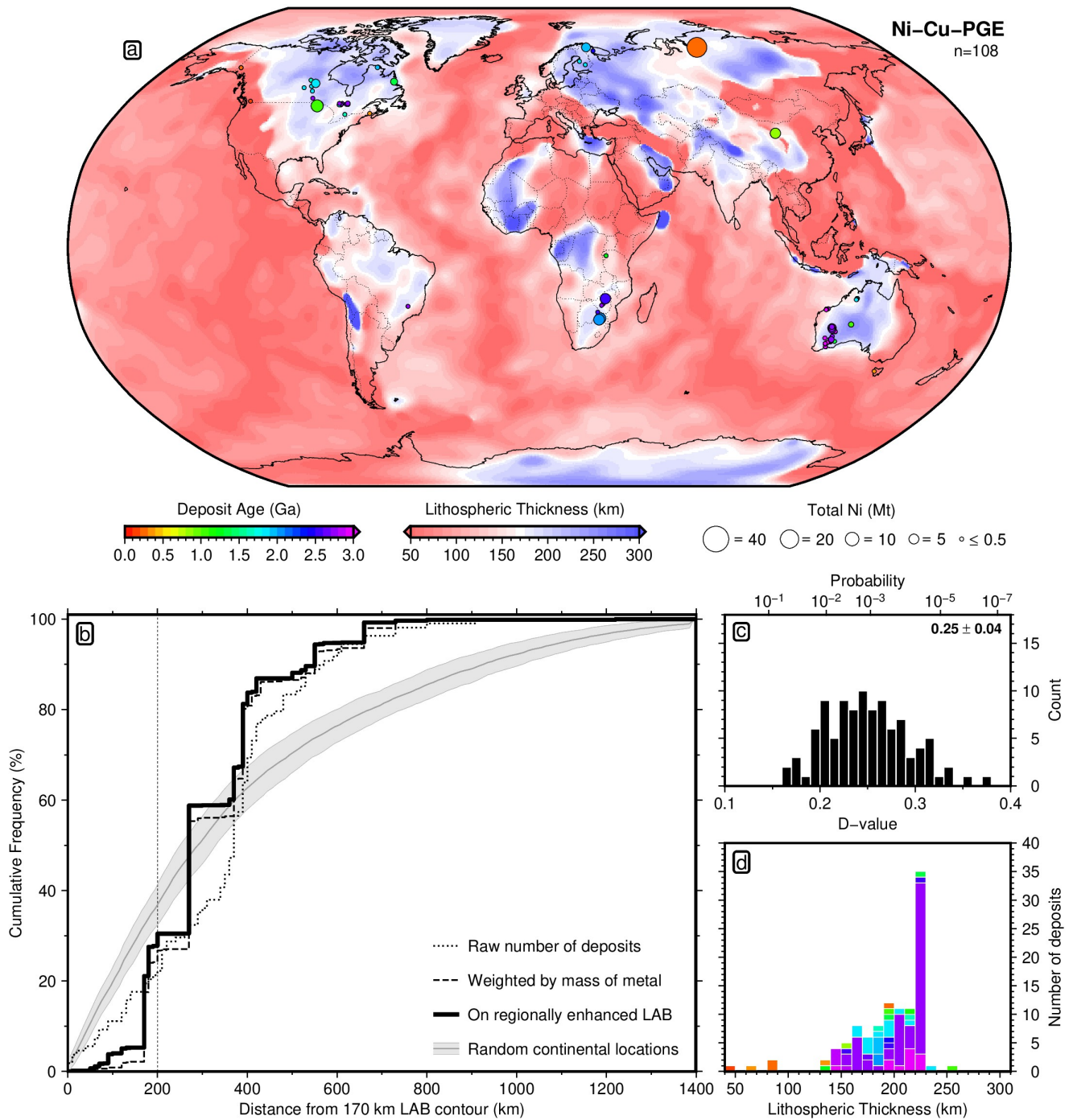


Figure S19: **108 magmatic nickel-copper-platinum group element deposits.** (a) LAB derived from SL2013sv tomography model using a calibrated anelasticity parameterisation.^{17,15} Circles = deposit locations; area proportional to estimate of total contained mass of metal (MT = megatonnes); unknown deposit size given 0.5 Mt symbol; colour = ore body formation age (billion years); unknown age plotted in grey. (b) Different approaches for generating cumulative distribution functions. Dotted line = simple count of number of deposits with increasing distance from the 170 km contour in global LAB map; dashed line = weighting by contained mass of nickel; solid black line = mass of metal-weighted deposits where Australian LAB has been replaced with regionally enhanced map (Figure S8a); grey line/bounds = mean and standard deviation of 100 sets of equivalent number of randomly drawn continental locations, with respect to regionally enhanced LAB. (c) Histogram of 100 D-values calculated for each random test set and a non-mass-weighted, locally enhanced CDF; inset lists mean and standard deviation of D-values; associated probabilities shown across top. (d) Histogram of deposit occurrence as a function of lithospheric thickness, coloured by deposit age.

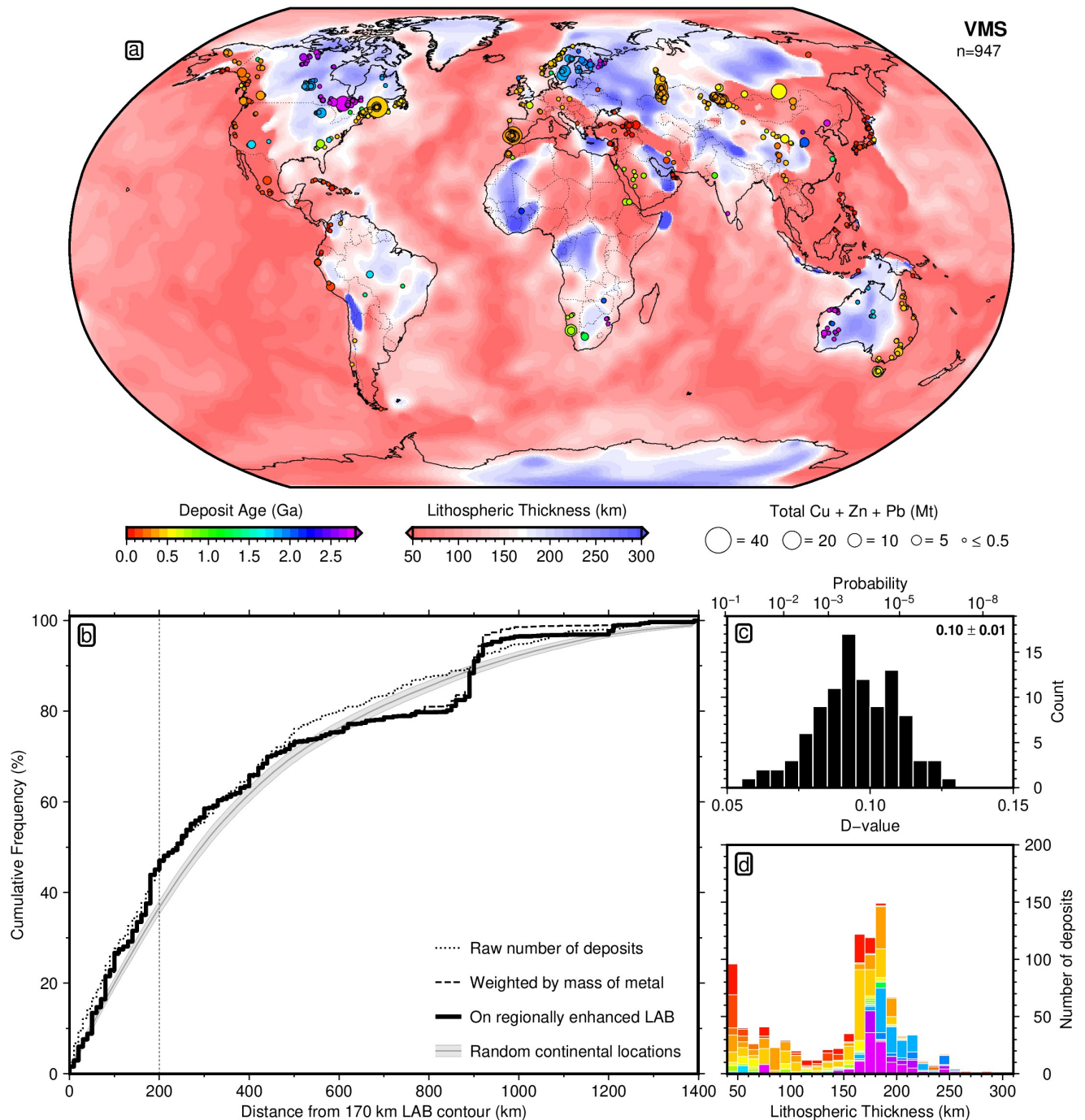


Figure S20: **947 volcanogenic massive sulphide deposits.** (a) LAB derived from SL2013sv tomography model using a calibrated anelasticity parameterisation.^{17,15} Circles = deposit locations; area proportional to estimate of total contained mass of metal (MT = megatonnes); unknown deposit size given 0.5 Mt symbol; colour = ore body formation age (billion years); unknown age plotted in grey. (b) Different approaches for generating cumulative distribution functions. Dotted line = simple count of number of deposits with increasing distance from the 170 km contour in global LAB map; dashed line = weighting by contained mass of copper, lead and zinc; solid black line = mass of metal-weighted deposits where Australian LAB has been replaced with regionally enhanced map (Figure S8a); grey line/bounds = mean and standard deviation of 100 sets of equivalent number of randomly drawn continental locations, with respect to regionally enhanced LAB. (c) Histogram of 100 D-values calculated for each random test set and a non-mass-weighted, locally enhanced CDF; inset lists mean and standard deviation of D-values; associated probabilities shown across top. (d) Histogram of deposit occurrence as a function of lithospheric thickness, coloured by deposit age.